

Chapter 4

Free Surface Singularities: From Singular Points to Spatio-Temporal Complexity



Jens Eggers

Abstract I use interfacial flows as an introduction to self-similar phenomena and scaling, my main examples being optics (wave fronts), and thin film dynamics. I describe how similarity solutions can be used to describe singular behavior in higher dimensions, where in general different spatial directions are characterized by different scaling behavior. I then show how singular solutions develop complexity through a sequence of instabilities. Combining chaotic dynamics with a higher-dimensional description, one obtains a mechanism for spatial complexity, as it is characteristic for turbulent flows.

4.1 Introduction and Overview

Free surfaces are a playground for nonlinear and emergent phenomena. One can classify singularities roughly as being time dependent, such as the breakup of a fluid drop, or being time-independent or persistent, such as the bright “caustic” lines one finds looking inside a coffee cup. It is not clear this distinction is even useful, but let us for the moment use it on physical grounds. For us singularities are points where some quantity or a derivative thereof diverges, at least in some limit. We want to argue that these are the crucial points around which everything else is organized.

4.1.1 Time-Dependent Singularities

In Fig. 4.1 we show the formation of a drop, which separates because surface tension favors reduction of the surface area. The initial splash from which the drop forms is produced by the impact of a drop into a glass of water, which produces its own complicated dynamics. However, the expectation is that when the typical size of the

J. Eggers (✉)
School of Mathematics, University of Bristol, Bristol, UK
e-mail: jens.eggers@bris.ac.uk

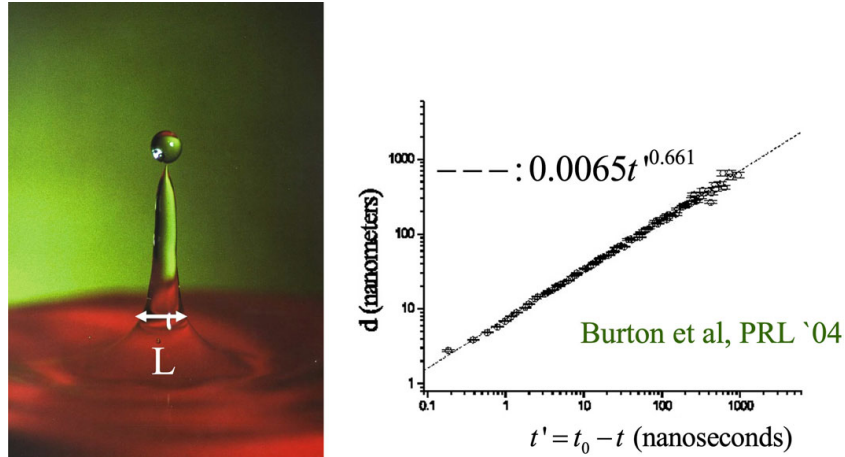


Fig. 4.1 Left: a drop is pinching off from a splash produced by an impacting drop (Edgerton, 1977). Right: In a different experiment, a drop of mercury is pinching off. Using an electrical measurement, the neck diameter is shown to behave close to $d \propto (t_0 - t)^{2/3}$, see Burton et al. (2004)

fluid neck separating the drop and the splash has become much smaller than a typical external scale L , its dynamics become independent of the means by which they have been produced. Such a decoupling suggests that the local dynamics becomes *scale invariant*, which is indeed confirmed by the power law behavior of the neck diameter as a function of the time $t_0 - t$ to breakup at the right of Fig. 4.1.

For a fluid of low viscosity like water, the motion, driven by surface tension γ , is opposed by inertia, which can be quantified by the density ρ of the liquid. Then dimensional analysis suggests that the minimum radius h_{\min} of the neck is

$$h_{\min} = C \left(\frac{\gamma(t_0 - t)^2}{\rho} \right)^{1/3} : \quad (4.1)$$

a $2/3$ power law, as confirmed by the experiment shown on the right of Fig. 4.1. In fact, the dimensionless prefactor $C \approx 0.7$ is also universal: independent of the geometry or of the type of fluid (as long as viscous effects can be neglected). We will however see below that there are numerous examples in which scale invariance can be broken. Nevertheless, let us emphasize that the typical structure of a singularity is *self-similar*. Another thought is that singularities represent the *fingerprint* of a PDE: they summarize what can be said about the “internal” structure of a PDE, independent of boundary or initial conditions.

Figure 4.2 shows the reverse process of two drops of water coalescing; without going into detail, this process is rather different from breaking. An energy balance yields for the minimum radius r_m of the bridge joining the two drops (Eggers et al., 1999):

$$r_m = C_i \left(\frac{\gamma R}{\rho} \right)^{1/4} t^{1/2}, \quad (4.2)$$

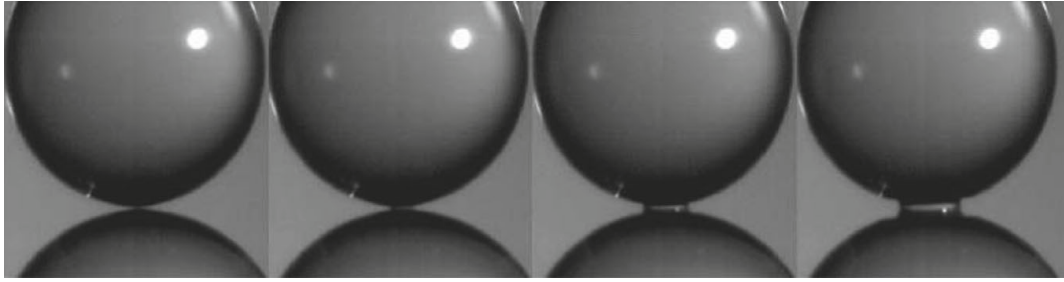


Fig. 4.2 Coalescence of two drops of water, see Aarts et al. (2005)

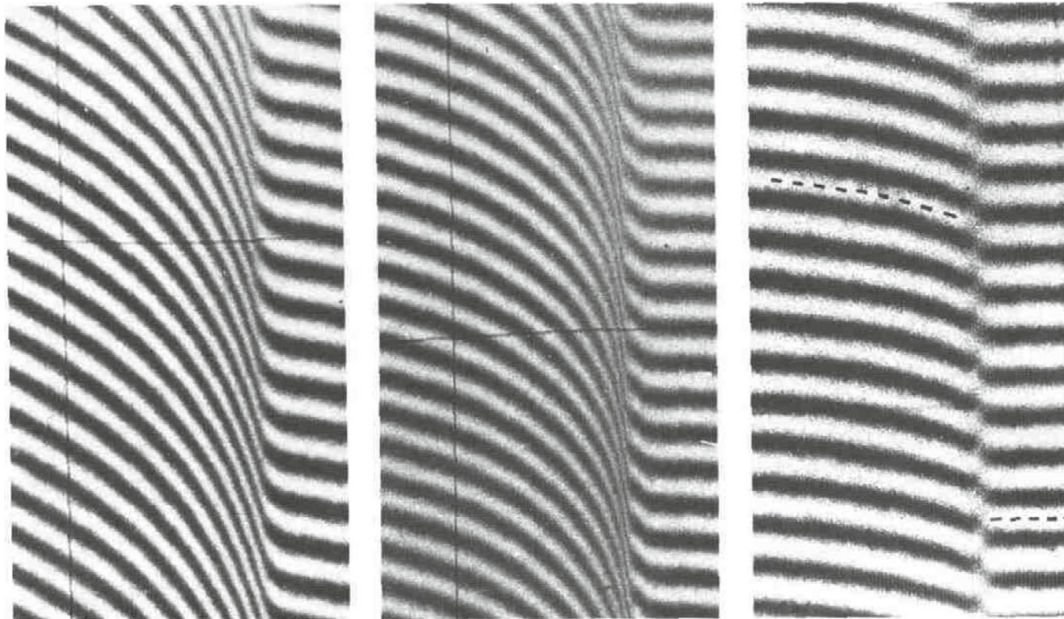


Fig. 4.3 The formation of a jump in density in a shock tube (Griffith & Bleakney, 1954). The interference fringes represent constant density. In the last panel, a jump in the density has occurred: a shock

and where t counts from the moment of reconnection. Notice that the drop radius R comes into play, so one is not constrained to the exponent $2/3$ as in the case of inviscid breakup: in fact, the exponent is now $1/2$!

The formation of a shock wave, shown in Fig. 4.3, provides a link between time-dependent and persistent singularities. Going from the first to the second panel, one observes a steepening of the density profile, owing to the non-linear character of the equations. In the third panel, a shock has formed, namely a discontinuous jump in the density profile; this persistent structure then continues to propagate.

Figure 4.4 presents an overview of cusp singularities, at which the surface is deformed in such a way that it ends in a point, with the two sides being asymptotically parallel. What is remarkable is that shapes of this same type are seen in very different physical systems. In the first example, the cusp forms on the surface of a viscous liquid, which is wrapped around an impacting jet. In actual fact, the tip of the cusp will be slightly rounded, owing to surface tension. Similar cusps are formed by the

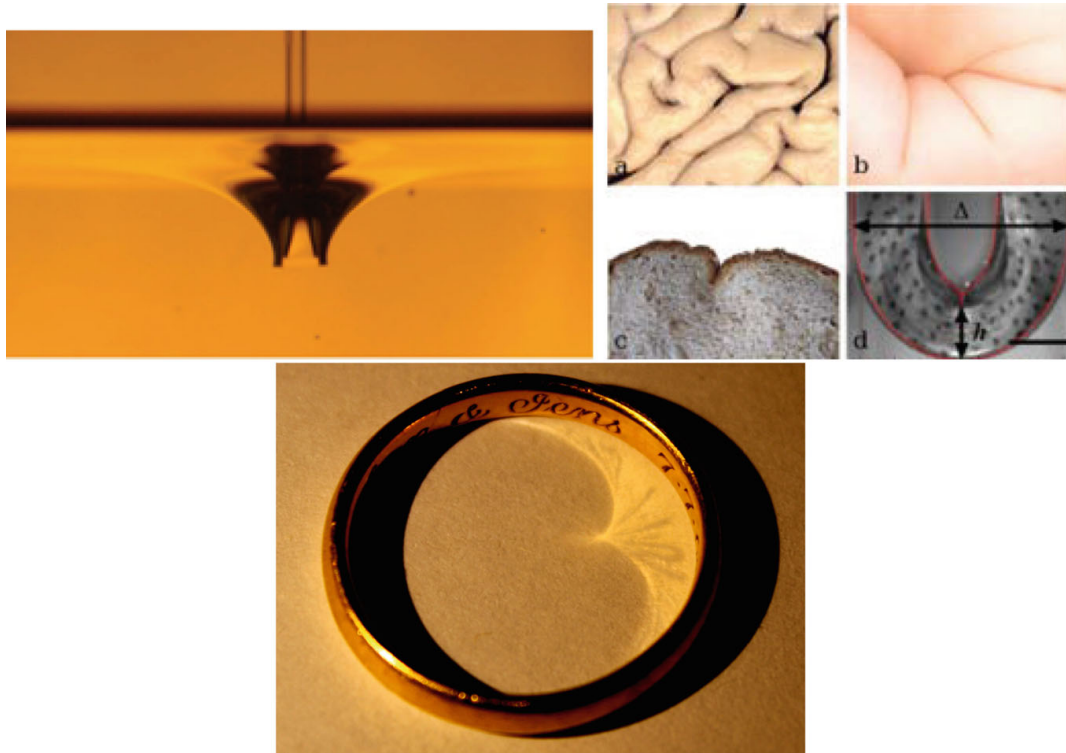


Fig. 4.4 An illustration of the “super-universality” of cusps. upper left: a cusp formed by the impact of a jet onto a viscous fluid (Reyssat et al., 2008); upper right: various cusp-shaped folds in elastic media (Hohlfeld & Mahadevan, 2011); bottom: a cusp caustic (Eggers & Fontelos, 2015)

folds of an elastic material, as seen on the right. Given the similarities between the equations of (linear) elasticity and viscous fluid dynamics, this is perhaps not so surprising. What is remarkable is that the same kind of cusps are formed by caustics, i.e. lines of bright light in the reflection pattern of light (see the bottom of the figure). We will come back to the description of caustics below.

The cusps shown above are essentially two-dimensional objects (although the cusp structure may be *unfolded* to some degree into the third dimension). In that sense an axisymmetric tip (see Fig. 4.5) is a simple three-dimensional analogue of the cusp. Again, there is a remarkable variety of such tips, although it turns out that not all of these cone-like structures are the same. While the “Taylor cone”, formed by electric fields, is indeed a perfect cone, the opening angle of the fluid structures is not strictly constant, but varies logarithmically with the distance from the tip (Courrech du Pont & Eggers, 2020).

4.1.2 Summary of Fundamentals

Let us summarize what we have learned, and let us also have some preview of things to come:

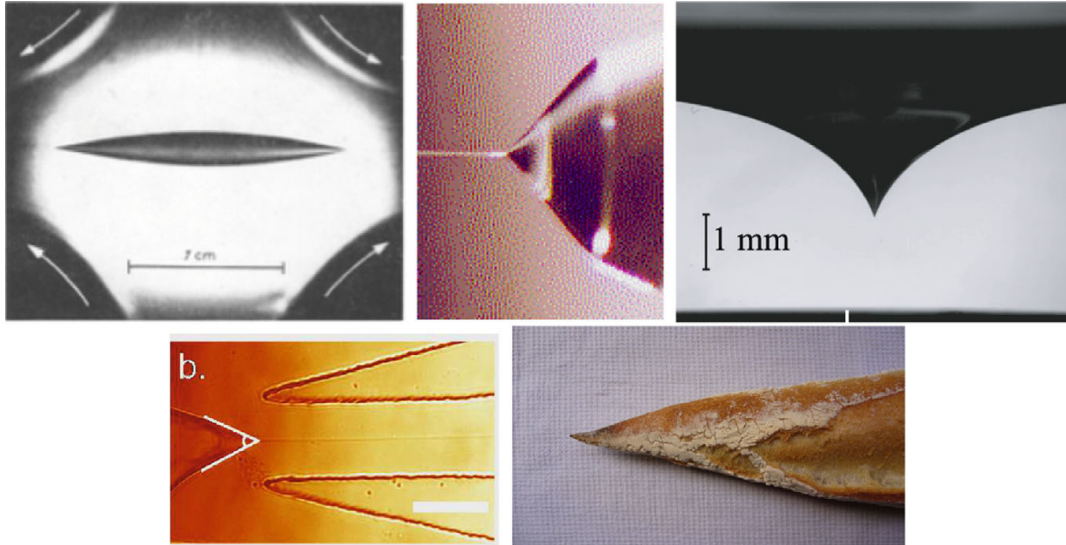


Fig. 4.5 Conical tips are seen very widely in fluid mechanics. Clockwise from the upper left: A pointed drop in an extensional flow (Taylor, 1934); a Taylor cone (Pantano et al., 1994); the surface of a viscous liquid emptying from a container (Courrech du Pont & Eggers, 2006); the pointed end of a French bread (Eggers and Villermaux, 2008); a cone in a flow focusing device (Dong et al., 2018)



Fig. 4.6 On the left, the breakup of a jet: the singular solution around the point of breakup is completely universal, i.e. independent of parameters like the jet radius, or the kind of fluid. On the right, a thin liquid film forms a bubble. Since surface tension is no longer a driving force toward breakup, other non-linear mechanisms come to the fore. As a result, the means by which a film breaks is highly non-universal, and even fundamental quantities like power laws depend on the mode of breakup (Bertozi et al., 1994; Kitavtsev et al., 2018)

1. Singularities are a recipe for new behavior and new structures to be created. For example, at a pinch-off singularity a new structure, a drop, is formed.
2. Singularities are the “fingerprint” of a non-linear PDE, in that they reveal the local structure of a solution. In some cases, this means that the singularity is universal, as in the breakup of a fluid jet, see Fig. 4.6, left: there are no free parameters in the solution, once it is written in “natural” units, determined by the type of fluid, $\ell_\nu = \nu^2 \rho / \gamma$ as the length scale, and $t_\nu = \nu^3 \rho^2 / \gamma^2$ as the time scale.

The situation is very different for a sheet, as seen on the right of Fig. 4.6. In that case, no “natural” mechanism for breakup exists, since a flat sheet minimizes the surface area. Instead, breakup needs to be provoked from the boundary, or there are additional variables. As a result, the singularity can be very different in different circumstances, and even the value of exponents can depend on the way the singularity is driven. Correspondingly, the equation allows for singular solutions with a great number of free parameters.

3. The fundamental structure of a singularity is determined by self-similarity. This means that a typical size ℓ of the singularity follows the scaling law

$$\ell = \ell_0(t_0 - t)^\alpha \equiv \ell_0 t'^\alpha : \quad (4.3)$$

a power law, where α is the similarity exponent. If there is a change in scale, i.e. ℓ is now measured with a different measuring stick, s times as long, we now have ℓ/s , and

$$\ell/s = \ell_0 \left(\frac{t'}{s^{1/\alpha}} \right)^\alpha .$$

In other words, a change in length scale can be absorbed into a change in time scale: the scaling law remains invariant, as expected from a law lacking a characteristic length scale.

4. There are many different ways in which the scaling law (4.3) can be relaxed. For example, for the collapse of a cylindrical cavity it was found (Eggers et al., 2007) that $\ell \propto t'^{\alpha(\tau)}$, where the exponent is now a slowly (logarithmically) varying function of time. Namely, if $\tau = -\ln |t'|$ is the logarithmic time distance to the singularity, it was found that $\alpha = 1/2 + 1/\sqrt{\tau}$, see Eggers et al. (2007). This means that the dynamics retain a (weak) “memory” of from where they started. In particular, the observed exponent now depends on the initial condition, for example the aspect ratio of the original cavity.
5. An even more interesting form of similarity is known as *discrete self-similarity* (Choptuik, 1993). An example is

$$\ell = t'^\alpha \left[1 + b \cos \frac{2\pi\tau}{T} \right];$$

this means the length ℓ returns to the same place (up to a rescaling in size) only after a period $\Delta\tau = T$. More exotic non-periodic versions can also be observed: $\ell = t'^\alpha g(\tau)$, where g is a non-periodic, possibly chaotic function.

The conclusion of this is that there are mechanisms for spatially localized singularities to produce temporally complex results (as if new music was invented all the time as one proceeds downward in scale). However, this is not yet a recipe for spatially complex structures.

6. Instead a one-dimensional structure can be spread out into higher dimensions by the mechanism of unfolding. Consider a singularity that is developing along

the x -axis. But since the initial condition is not uniform in the y -direction, the singularity time $t_c(y)$ will be a function of y :

$$\ell = \ell_0 (t - t_c(y))^\alpha .$$

If the singularity occurs for $y = 0$ first, we must have the expansion $t_c = t_0 + ay^2 + \dots$ (if there were a linear term, it would mean the singularity occurred away from $y = 0$ first). But this means the singularity has a characteristic size $t'^{1/2}$ in the y -direction.

7. We will see that by combining the above mechanism for unfolding into higher dimensions with complex temporal dynamics, one obtains a mechanism for producing complex “turbulent” patterns.
8. A central role in the understanding of singularities is played by asymptotics, investigating the limit $t' \rightarrow 0$, which controls the *local* behavior. This local behavior needs to be embedded into a *global* environment (for example, boundary conditions need to be satisfied). The condition that local and global behaviors are consistent leads to a problem in matched asymptotics. However, often (in the case of universal singular behavior) it is sufficient to demand that the solution at a fixed distance δ from the singularity has a finite limit as $t' \rightarrow 0$.

4.2 Similarity Solutions

The principles laid out above suggest we are looking for so-called similarity solutions of the form

$$h(x, t) = t'^\alpha H(\xi), \quad \xi = \frac{x'}{t'^\beta}, \quad (4.4)$$

where $t' = t_0 - t$ and $x' = x - x_0$. This means that as the singularity is approached, its shape remains the same, only its extension $\ell \propto t'^\beta$ and size $h \propto t'^\alpha$ are rescaled. Let us illustrate this using a simple equation, modeling the flow of a film of liquid on a solid substrate.

4.2.1 The Thin Film Equation

Let us consider a thin film of liquid on a substrate (Blossey, 2012; Craster & Matar, 2009; Oron et al., 1997). We assume that inertia is not important, so we want to solve Stokes' equation

$$\nabla p = \eta \Delta \mathbf{v},$$

where η is the viscosity. The idea is to assume that the flow is locally parallel, so we write $\mathbf{v} = u(z)\mathbf{e}_x$; inserting this into the Stokes equation we have $\eta u'' = p_x$. Note

that we are assuming that the pressure is constant through the layer, a hallmark of lubrication theory. The boundary conditions are those of no slip on the solid surface, $u(0) = 0$, and of vanishing shear stress at the free surface $z = h$. In the limit of an almost flat interface this amounts to $u'(h) = 0$. As a result, we can solve for the profile to find

$$u(z) = \frac{p_x}{2\eta} z(z - 2h), \quad (4.5)$$

a quadratic profile!

It follows from mass conservation that the film thickness changes according to $h_t + Q_x = 0$, where

$$Q = \int_0^h u dz = \frac{p_x h^3}{3\eta}$$

is the mass flux, so that finally we have the thin film equation

$$h_t = \frac{1}{3\eta} (p_x h^3)_x. \quad (4.6)$$

To close the equation, we need the pressure. The contribution from surface tension is $p = -\gamma h_{xx}$, with γ the surface tension coefficient. This alone can never lead to breakup, as surface tension only favors flattening of the profile. Instead, we need to consider an attractive interaction between the free surface and the substrate, which comes from the long-ranged interactive forces between molecules, which decay like $1/\text{distance}^6$. Thinking in terms of the energy (from which the pressure is retrieved by differentiating with respect to $h(x)$), we have to perform a double integral over all interactions. A local contribution from near the interface results in the surface tension contribution given above. If however the film thickness is comparable to the range of the interaction, there is also a contribution coming from the interaction between liquid and substrate molecules. For a flat interface, the integral can be performed and leads to Blossey (2012):

$$p = -\gamma h_{xx} + \frac{A}{6\pi h^3}, \quad (4.7)$$

where A is known as the Hamaker constant.

One observes immediately that now for h small the pressure becomes large, so fluid is pushed out from thin regions, making the layer even thinner. This ultimately leads to localized breakup. The exponent $n = 3$ in (4.6) is known as the mobility exponent, the exponent $m = 3$ in (4.7) characterizes the range of the interaction. In order to create a playing field in which to explore many different kinds of dynamics, we will from now on treat both exponents as *free parameters*. There are physical systems for which different parameter values can indeed be argued, but here we only treat this as a mathematical laboratory. In other words, we have (after scaling, so that prefactors are normalized to unity):

$$h_t - (h^n p_x)_x = 0, \quad p = -h_{xx} + \frac{h^{-m}}{m}; \quad (4.8)$$

in the classical case, $n = m = 3$. Combining the two equations, we arrive at the compact form

$$h_t + (h^n h_{xxx} + h^{n-m-1} h_x)_x = 0. \quad (4.9)$$

So far, we have assumed that the film thickness only varies in a single direction x . For a film on a two-dimensional substrate with coordinates x and y , it is natural to generalize (4.9) to an equation for $h(z, y, t)$ (Bertozzi & Pugh, 1994)

$$h_t = -\nabla \cdot (h^n \nabla \Delta h + h^{n-m-1} \nabla h), \quad (4.10)$$

which is isotropic in x, y .

4.2.2 Linear and Non-linear Solutions

To gain some insight into the driving forces, we consider the linear stability of a flat film of thickness h_{ref} , adding small perturbations of size ϵ . For simplicity, we only allow for perturbations in the x -direction and linearize:

$$h(x, t) = h_{\text{ref}} + \epsilon e^{\omega t + ikx}, \quad (4.11)$$

where ω is the growth rate of the perturbation. Inserting (4.11) into (4.9), we obtain the dispersion relation

$$\omega = h_{\text{ref}}^{n-m-1} k^2 (1 - h_{\text{ref}}^{m+1} k^2). \quad (4.12)$$

One observes that wavenumbers $k < h_{\text{ref}}^{-(m+1)/2}$ are unstable, while shorter wavelengths lead to complex ω and are stable. The reason is that more surface area is produced for shorter wavelengths, so these perturbations are not energetically favorable. This type of instability was investigated by Rayleigh in the context of the breakup of a fluid jet. The highest growth rate is achieved for $k = h_{\text{ref}}^{-(m+1)/2} / \sqrt{2}$, which is known as the Rayleigh mode. Its significance lies in the fact that this wavelength will be observed for a *random* initial perturbation.

As perturbations grow for the unstable modes, nonlinear effects eventually take over. The idea is that for a locally driven pinch-off singularity, $h \rightarrow 0$ and $\ell \rightarrow 0$, so that as $t \rightarrow t_0$, $h \propto t'^\alpha$, and $\ell \propto t'^\beta$. This leads to the similarity solution (4.4), for which the exponents α, β , as well as the profile $H(\xi)$ still need to be found. First, the exponents are found by balancing the terms in (4.9). For every factor of h , there is a factor of t'^α , a factor of $t'^{-\beta}$ for every space derivative, and t'^{-1} for a time derivative. This leads to the balance of powers of t' :

$$\alpha - 1 = (n + 1)\alpha - 4\beta = (n - m)\alpha - 2\beta,$$

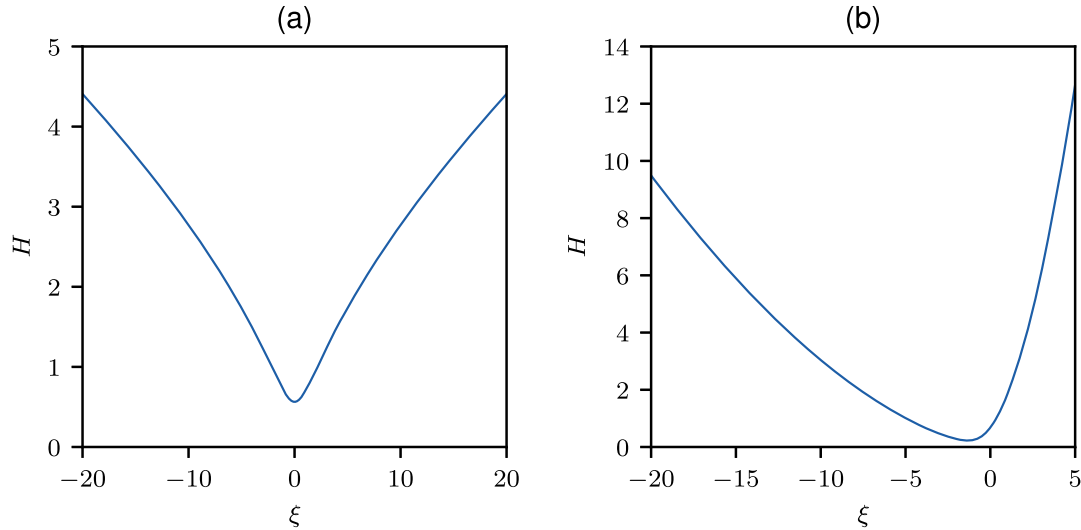


Fig. 4.7 Two examples of similarity solutions (solutions of (4.14)) for different values of n, m . **a** a regular, symmetric similarity solution for $n = 3, m = 2$. **b** a regular, asymmetric solution for $n = 1.5, m = 0.2$

and thus

$$\alpha = \frac{1}{2 + 2m - n}, \quad \beta = \frac{1 + m}{4 + 4m - 2n}, \quad (4.13)$$

in terms of the parameters n and m . This situation is known as self-similarity of the first kind.

Using these values, we can plug (4.4) into (4.9) to obtain the similarity equation:

$$-\alpha H + \beta \xi H_\xi = -[H^n H_{\xi\xi\xi} + H^{n-m-1} H_\xi]_\xi. \quad (4.14)$$

In order to solve (4.14), one needs boundary conditions, which come from the matching requirement that since $\ell \rightarrow 0$ as $t' \rightarrow 0$, we expect $h(x, t) \rightarrow h(x, 0)$ as t' goes to zero. In terms of (4.4), this means that for fixed x' (and thus $\xi \rightarrow \pm\infty$),

$$h(x, t) = t'^\alpha H\left(\frac{x'}{t'^\beta}\right)$$

approaches the finite value $h(x, 0)$. But this implies the boundary conditions

$$H(\xi) \rightarrow A\xi^{\alpha/\beta}, \quad \xi \rightarrow \pm\infty. \quad (4.15)$$

The constant A is in general not known, but is often a universal number which follows as part of the solution. This solution depends very much on the values of the parameters n, m . Two examples are shown in Fig. 4.7, where on the left we show a symmetric solution, on the right an asymmetric solution, so that left-right symmetry

is broken. Which of the two cases is observed (the one shown in Fig. 4.7 or a flipped one), is determined by the initial conditions.

But in fact this is an oversimplified picture! Typically, there is not just one solution (as shown in the figure), but a discretely infinite sequence, only the first member of which (which we call the ground state) is shown in Fig. 4.7.

To find out what distinguishes the different solutions, we need to discuss their *stability* (more about this later on). It turns out there are essentially two cases:

1. There is one stable “ground state” solution $H_0(\xi)$ and a sequence $H_i(\xi)$, $i \geq 1$, of unstable solutions.
2. all H_i are unstable, and other, slowly varying solutions are observed instead.

4.2.3 The Eikonal Equation

We begin with the underlying wave physics, described by the wave equation

$$\Delta\phi - c^{-2}\phi_{tt} = 0, \quad (4.16)$$

where c is the wave speed. For simplicity, we confine ourselves to a scalar field ϕ (we disregard polarization etc.). A monochromatic wave of angular frequency ω is described by

$$\phi = \Phi e^{-ikct}, \quad (4.17)$$

where $k = \omega/c$ is the wave number. Inserting (4.17) into (4.16), we obtain the Helmholtz equation

$$\Delta\Phi + k^2\Phi = 0. \quad (4.18)$$

The solution will have very rapid spatial oscillations, while we are interested in phase changes on the large scale. To bring them out, we look at

$$\Phi = \Phi_0(\mathbf{x}) \exp\{ik\psi(\mathbf{x})\}, \quad (4.19)$$

and study the limit of large k . Here $\psi(\mathbf{x})$ is the phase of the wave, and $\Phi_0(\mathbf{x})$ its amplitude. To leading order we obtain

$$k^2\Phi_0(1 - (\nabla\psi)^2) + O(k) = 0$$

so that we obtain a nonlinear equation for the phase:

$$|\nabla\psi|^2 = 1, \quad (4.20)$$

which is known as the eikonal equation. It describes the three-dimensional shape of surfaces of constant phase.

To turn this into a time-dependent problem, in analogy to the thin film equation studied earlier, we consider the propagation in time of a wave front, for example after a light source was switched on. Such a propagation is described by $\psi(\mathbf{x}) = ct$, where $\psi(\mathbf{x})$ is found from (4.20). We can turn this into a PDE for the propagation of a graph $z(\mathbf{x}_{\parallel}, t)$, where z is the direction of propagation and \mathbf{x}_{\parallel} are the transversal coordinates. As a result, $\psi(\mathbf{x}_{\parallel}, z(\mathbf{x}_{\parallel}, t)) = ct$. We differentiate that with respect to t and with respect to \mathbf{x}_{\parallel} , which results in

$$c = \psi_z \dot{z}, \quad \nabla_{\parallel} \psi + \psi_z \nabla_{\parallel} z = 0.$$

Squaring the first equation and using (4.20) we have

$$c^2 = \psi_z^2 \dot{z}^2 = \dot{z}^2 (1 - \nabla_{\parallel} \psi^2) = \dot{z}^2 (1 - \psi_z^2 \nabla_{\parallel} z^2) = \dot{z}^2 (1 - c^2 \nabla_{\parallel} z^2 / \dot{z}^2),$$

so that

$$\dot{z}^2 = 1 - \nabla_{\parallel} z^2, \quad (4.21)$$

where we normalized the speed of light to unity. This is the dynamical form of the eikonal equation.

4.2.4 Wavefronts and the Caustic Condition

Apart from (4.21), there are at least two other equivalent ways of expressing the same physical information. This can also be viewed as ways to solve the differential equation (4.21). The first, known as Huygens' principle, is equivalent to saying that from each point of a wavefront emanates a ray which moves at constant speed ($c = 1$) in the normal direction. To construct the wavefront at future times t , one simply has to connect the points to which each individual ray has progressed. To be explicit, write a surface in D dimensions as $\mathbf{x}(\mathbf{u}, t)$, where \mathbf{u} is a $d - 1$ -dimensional vector parameterizing the surface, and thus parameterizing rays. Thus the Huygens solution is ($c = 1$)

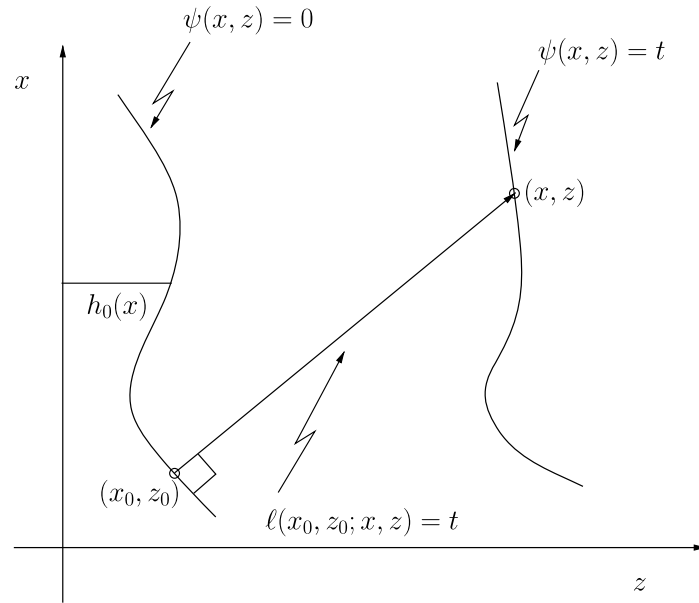
$$\mathbf{x}(\mathbf{u}, t) = \mathbf{x}(\mathbf{u}, 0) + \mathbf{n}(\mathbf{u}, 0)t, \quad (4.22)$$

where $\mathbf{n}(\mathbf{u}, 0)$ is the normal to the initial wave front. From this a new wave front at time t can be constructed, as illustrated in Fig. 4.8.

To obtain an explicit solution $h(\mathbf{x}, t)$ to (4.20) in parameterized form, let $h(\mathbf{u}, 0) = h_0(\mathbf{u})$ be the graph representation of the initial wave front, so that $\mathbf{x}(\mathbf{u}, 0) = (\mathbf{u}, h_0(\mathbf{u}))$. Then, computing the normal vector as $\mathbf{n}(\mathbf{u}, 0) = (-\nabla h_0, 1) / \sqrt{1 + \nabla h_0^2}$, we find the solution

$$h = h_0(\mathbf{u}) + \frac{t}{\sqrt{1 + \nabla h_0^2}}, \quad \mathbf{x}_{\parallel} = \mathbf{u} - \frac{\nabla h_0}{\sqrt{1 + \nabla h_0^2}} t. \quad (4.23)$$

Fig. 4.8 A wavefront can be described either as the graph of a function $z = h(x, t)$, or as lines of constant value of the action $S(x, z)$. Rays are perpendicular to the wavefronts, and $\ell(x_0, z_0; x, z)$ measures the optical path length between two points



It can be checked by substitution that (4.23) is indeed the desired solution of (4.20) with initial condition $h(\mathbf{x}_{\parallel}, 0) = h(\mathbf{x}_{\parallel})$. The key observation is that for a smooth initial condition $\mathbf{x}(\mathbf{u}, 0)$, each component of (4.22) is a smooth function for all t . Singularities in the shape of the wave front can only arise if the mapping $\mathbf{u} \mapsto \mathbf{x}$ no longer has full rank, which is precisely the situation described by catastrophe theory (Nye, 1999).

In catastrophe theory, Fermat's principle is often used to describe singularities of wave fronts. The advantage is that one only has to deal with a single scalar function ℓ , the light distance between two points, see Fig. 4.8. Namely, the distance between a point on the initial wave front $\mathbf{x}(\mathbf{u}, 0) = (\mathbf{u}, h_0(\mathbf{u}))$ and a point $(\mathbf{x}_{\parallel}, z)$ is

$$\ell = [(\mathbf{x}_{\parallel} - \mathbf{u})^2 + (z - h_0(\mathbf{u}))^2]^{1/2}. \quad (4.24)$$

Now the wave front $\mathbf{x}(t) = (\mathbf{x}_{\parallel}(t), z(t))$ is determined by the extremal condition (Fermat's principle)

$$\nabla_{\mathbf{u}} \ell = 0 \quad (4.25)$$

and

$$\ell = ct. \quad (4.26)$$

Indeed, it can be checked directly that (4.25) and (4.26) are equivalent to (4.23) ($c = 1$), and thus to (4.20).

Now let us characterize singular points (caustics) in terms of Fermat's principle. We write the initial wave front as a graph $z(x, y, 0) \equiv h_0(x, y)$ over the x, y -plane; $\mathbf{u} = (\varphi, \psi)$ parameterizes the initial wave front. Then the wave front at a time t can be written as

$$\mathbf{x}(\varphi, \psi, t) = (x(\varphi, \psi, t), y(\varphi, \psi, t), z(\varphi, \psi, t)),$$

where

$$\ell(x, y, z, \varphi, \psi) = [(\varphi - x)^2 + (\psi - y)^2 + (z - h_0(\varphi, \psi))^2]^{1/2} \quad (4.27)$$

is the optical distance. On a wavefront, the conditions

$$\ell_\varphi = \ell_\psi = 0, \quad \ell = t \quad (4.28)$$

are satisfied. Differentiating the first two equations with respect to φ and ψ , we obtain

$$\begin{pmatrix} \ell_{\varphi\varphi} & \ell_{\varphi\psi} \\ \ell_{\varphi\psi} & \ell_{\psi\psi} \end{pmatrix} = - \begin{pmatrix} x_\varphi & y_\varphi & z_\varphi \\ x_\psi & y_\psi & z_\psi \end{pmatrix} \begin{pmatrix} \ell_{\varphi x} & \ell_{\psi x} \\ \ell_{\varphi y} & \ell_{\psi y} \\ \ell_{\varphi z} & \ell_{\psi z} \end{pmatrix}. \quad (4.29)$$

A caustic occurs where ℓ has a saddle point, which is where rays concentrate. This means that at the points of the caustic, the Hessian determinant of ℓ vanishes. This certainly happens if the Jacobi matrix of the surface $\mathbf{x}(\varphi, \psi)$ no longer has full rank, i.e. at singularities of the wave front. In other words, condition for a caustic is that

$$H = \ell_{\varphi\varphi}\ell_{\psi\psi} - \ell_{\varphi\psi}^2 = 0. \quad (4.30)$$

The mapping $\mathbf{x}(\varphi, \psi)$ no longer having full rank is equivalent to the minors D_1, D_2, D_3 of the Jacobi matrix vanishing. Differentiating $\ell(\mathbf{x}(\varphi, \psi), \varphi, \psi) = t$, with respect to φ and ψ , and using $\ell_\varphi = 0$ and $\ell_\psi = 0$, respectively, it follows that the columns of the matrix are linearly dependent. Thus

$$D_1 = x_\varphi y_\psi - x_\psi y_\varphi = 0 \quad (4.31)$$

is equivalent to all three minors vanishing, which is equivalent to (4.30).

4.2.5 The Cusp

We now come back to a similarity description of the singularities of wavefronts. We insert the ansatz

$$z = t + |t|^\alpha h(\xi), \quad \xi = \frac{x}{|t|^\beta} \quad (4.32)$$

into (4.21), where we take the singularity to occur at $t = 0$. The first term proportional to t arises because the wave propagates at constant speed c (normalized to one) in the z -direction. Inserting into (4.21), we obtain to leading order:

$$\mp 2|t|^{\alpha-1} (-\alpha h + \beta \xi h_\xi) + |t|^{2\alpha-2\beta} h_\xi^2 = 0, \quad (4.33)$$

which means that $\beta = (\alpha + 1)/2$, while α is open. It will be obtained from a regularity condition on the solution; this situation is called self-similarity of the second kind.

The similarity equation becomes

$$2\alpha h - (\alpha + 1)\xi h_\xi \pm h_\xi^2 = 0. \quad (4.34)$$

Here and in the following, the upper sign refers to the time before the singularity: $t < 0$, which means that $|t| = -t$; the lower sign refers to $t > 0$. Putting $U = -h_\xi$, we obtain the semilinear equation

$$(\alpha - 1)U - (\alpha + 1)\xi U_\xi \mp U U_\xi = 0, \quad (4.35)$$

which is the same equation which describes a shock in the Burgers equation. A solution can be found using $\xi_U = (U_\xi)^{-1}$; alternatively, it is easy to check that the solution is

$$\xi = \mp U - C U^{\frac{\alpha+1}{\alpha-1}}. \quad (4.36)$$

The exponent must be an odd integer, otherwise the similarity profile *before* singularity formation would have a singularity at the origin (therefore it must be an integer), and it would not be one-to-one (therefore odd). In addition, the constant C must be positive. The value “1” is also not allowed, otherwise the solution would be a straight line, which does not match a finite outer solution. Thus we have $(\alpha + 1)/(\alpha - 1) = 2i + 3$, with $i = 0, 1, 2, \dots$. Of these solutions, only $i = 0$ corresponds to a stable “ground state” solution (we will investigate stability in the section below), so finally we have

$$\xi = \mp U - C U^3, \quad (4.37)$$

as shown in Fig. 4.9. The exponents are $\alpha = 2$ and $\beta = 3/2$.

Caustics (bright spots) are places where rays concentrate. These are points where the optical distance, as function of variables parameterizing the original wavefront, has a saddle point. Since U can be chosen as such a parameter, in one dimension this is the condition $\xi_U = 0$, see condition (4.31) below.

It is seen on the right of Fig. 4.9 that two such points appear. It follows that

$$\xi_U = 1 - 3C U^2 = 0,$$

and a caustic occurs for $U_{cr} = \pm 1/\sqrt{3C}$ or $\xi = \pm \xi_{cr} = U_{cr} - C U_{cr}^3$. But this means a caustic is traced out by $x = \pm \xi_{cr} t^{3/2}$ for $t > 0$, while traveling along the z -axis. Since $z = ct$, in space this traces out a cusp

$$x = \pm \xi_{cr} z^{3/2}, \quad (4.38)$$

as seen in a coffee cup, Fig. 4.10.

Returning to the shape of the wave front $h(\xi)$, we have

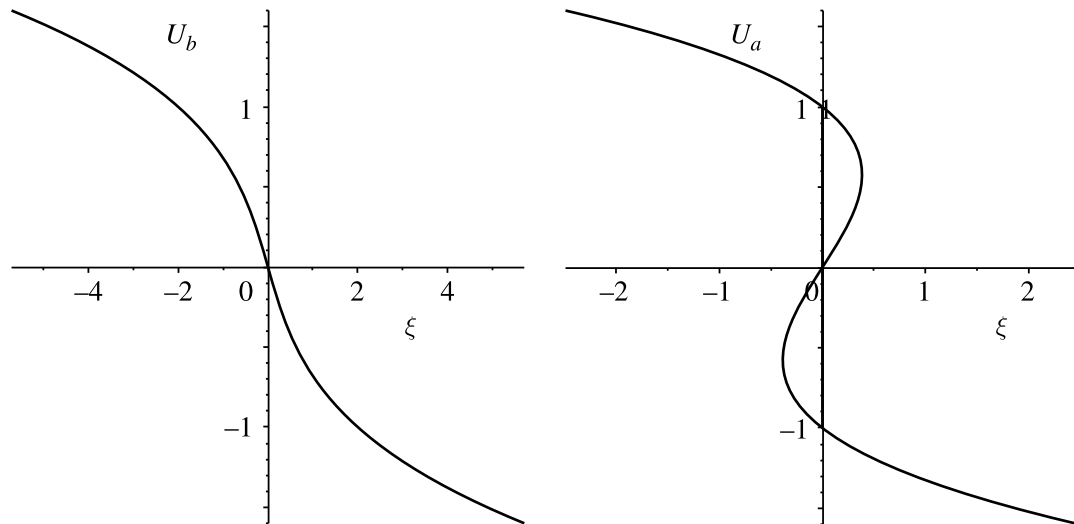
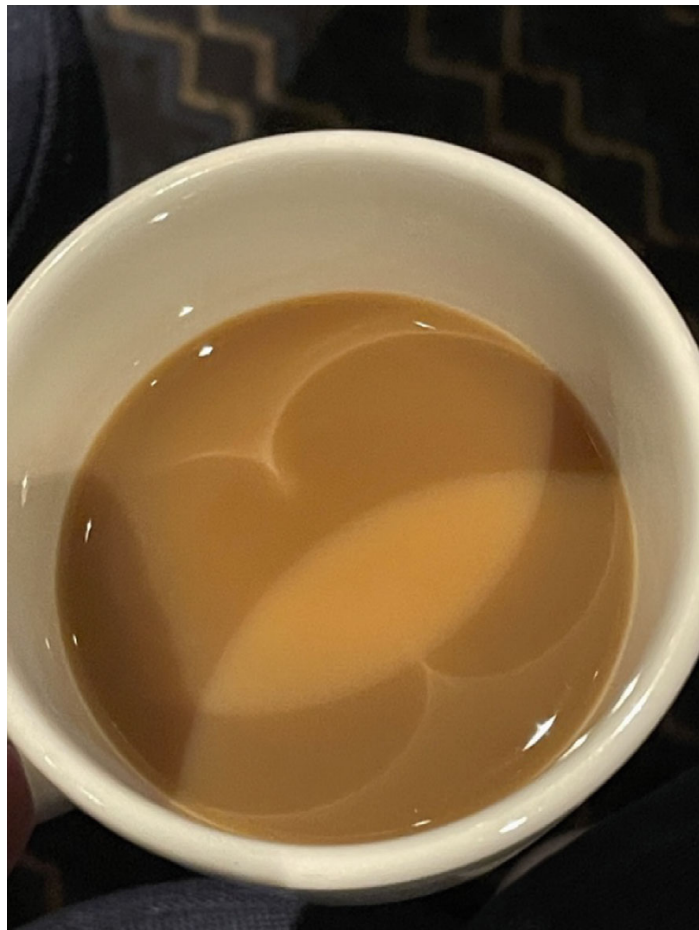


Fig. 4.9 Similarity solutions before and after the shock, according to (4.37). On the left, the solution before the singularity (upper sign); on the right, the solution after the singularity (lower sign). The two places where the profile is vertical on the right correspond to the caustic

Fig. 4.10 Bright caustic lines form a cusp in a coffee cup (photo courtesy of Ann Eggers)



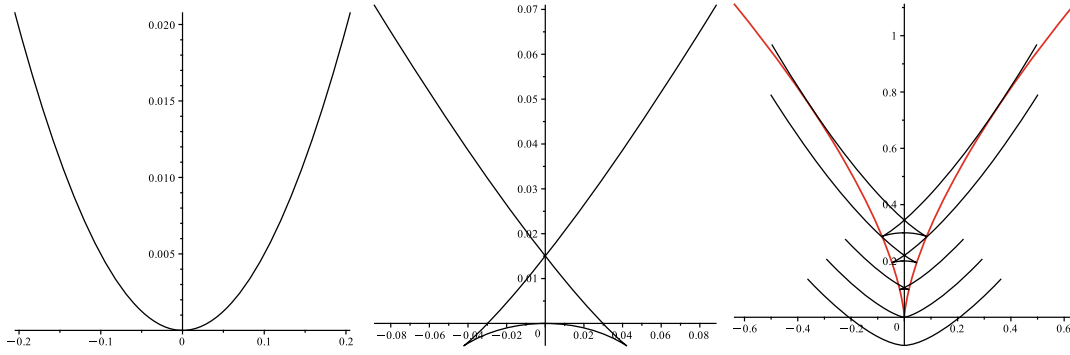


Fig. 4.11 The swallowtail similarity function (4.39) before the singularity (left) and after (middle). On the right, the swallowtail front is propagated as in (4.40)

$$h_U = \xi_U h_\xi = -\xi_U U = \pm U + 3CU^3.$$

We can integrate this as

$$h = \int^U (\mp U + CU^3) dU = \mp \frac{U^2}{2} + \frac{C}{4} U^4 + const.$$

Thus a parametric form of the wave front is given by

$$\xi = \mp U - CU^3, \quad h = \mp \frac{U^2}{2} + \frac{C}{4} U^4 + const, \quad (4.39)$$

which is also known as a swallowtail curve (Eggers & Suramlishvili, 2017). After the singularity, the wave front becomes singular, and forms cusp points. It is known generally (Nye, 1999) that these cusp points of the wave front trace out the caustic.

According to (4.32), in real space we have

$$z = t + |t|^2 h \left(\frac{x}{|t|^{3/2}} \right); \quad (4.40)$$

this is singular for $x_{cr} = \xi_{cr} t^{3/2}$, $z = t$, which traces out the cusp, see the right of Fig. 4.11.

4.3 Stability Analysis

4.3.1 General

Self-similar solutions are not always observed even if the similarity equation has solutions: those solutions may be unstable. To investigate, we look at the neighbor-

hood and probe the linear stability. This may seem difficult, since the solution whose stability we investigate is itself time-dependent. The trick is to allow $H(\xi)$ to vary on a logarithmic scale (Giga & Kohn, 1985):

$$h(x, t) = t'^{\alpha} H(\xi, \tau), \quad \xi = x'/t'^{\beta}, \quad \tau = -\ln t'. \quad (4.41)$$

Now given *any* equation of motion $h_t = F\{h\}$, where $F\{h\}$ contains derivatives h_x etc.), this has a similarity equation of the form

$$0 = \alpha H - \beta \xi H_{\xi} + F\{H\}.$$

Considering the additional dependence on τ ($\frac{\partial \tau}{\partial t} = 1/t'$ for $t' > 0$, before the singularity) this becomes

$$H_{\tau} = \alpha H - \beta \xi H_{\xi} + F\{H\}, \quad (4.42)$$

with the similarity solution being a fixed point of the “dynamical system” (4.42). Linearizing around the fixed point, this makes it easy to investigate the stability of the similarity solution, i.e. whether a certain self-similar behavior is actually observed. Later we will use the same equation to investigate more complex behavior, not strictly self-similar.

4.3.2 The Eikonal Equation

To illustrate the procedure, let us consider the stability of self-similar solutions to the eikonal equation, given by (see (4.32))

$$z = t + |t|^{\alpha} h(\xi, \tau), \quad \xi = \frac{x}{|t|^{\beta}}.$$

Since $\frac{\partial \tau}{\partial t} = \pm 1/|t|$ before/after the singularity the dynamical system becomes

$$h_{\tau} = \alpha h - \frac{\alpha + 1}{2} \xi h_{\xi} \pm \frac{h_{\xi}^2}{2} = 0. \quad (4.43)$$

This is simplified if differentiated with respect to ξ , and putting $U = -h_{\xi}$ we obtain

$$U_{\tau} = \frac{\alpha - 2}{2} U - \frac{\alpha + 2}{2} \xi U_{\xi} \mp U U_{\xi}, \quad (4.44)$$

or with $\alpha = (i + 2)/(i + 1)$ (and so $(\alpha + 1)/(\alpha - 1) = 2i + 3$ as above)

$$U_\tau = \frac{U}{2i+2} - \frac{2i+3}{2i+2} \xi U_\xi \mp U U_\xi, \quad i = 0, 1, 2, \dots$$

Now if $\bar{U}_i(\xi)$ is a solution to the similarity equation (4.35) (the base solution), then a perturbation has the form

$$U(\xi, \tau) = \bar{U}_i(\xi) + \delta e^{\nu\tau} P(\xi), \quad (4.45)$$

and we linearize in δ . Here ν is the eigenvalue and $P(\xi)$ the eigenfunction. This yields an eigenvalue equation for the perturbations P around the base profile \bar{U}_i (specializing to $t' > 0$):

$$\left(\frac{1}{2i+2} - \nu \right) P - \frac{2i+3}{2i+2} \xi P_\xi - P(\bar{U}_i)_\xi - P_\xi \bar{U}_i = 0, \quad i = 0, 1, \dots \quad (4.46)$$

Replacing ξ by \bar{U}_i as the independent variable, we find

$$P \left[\left(\frac{1}{2i+2} - \nu \right) (1 + (2i+3)\bar{U}_i^{2i+2}) + 1 \right] = \frac{\partial P}{\partial \bar{U}} \left[\frac{\bar{U}_i}{2i+2} + \frac{2i+3}{2i+2} \bar{U}_i^{2i+3} \right]. \quad (4.47)$$

This is solved by separation of variables:

$$P = \frac{\bar{U}_i^{3+2i-2\nu(i+1)}}{1 + (2i+3)\bar{U}_i^{2i+2}}. \quad (4.48)$$

The exponent $3 + 2i - 2\nu(i + 1)$ must be an odd integer for (4.48) to be regular at the origin, so the eigenvalues are

$$\nu_j = \frac{2i+3-j}{2i+2}, \quad j = 0, 1, 3, 5, \dots \quad (4.49)$$

Thus for the first similarity solution in the series ($i = 0$), the eigenvalues are $\nu = 3/2, 1, 0, -1, \dots$. Thus surprisingly, there are two *unstable* eigenvalues and one neutral one: the solution seems to be unstable! However, this is not the case; instead, the positive eigenvalues are a result of the fact that the origin x_0 and time t_0 can be chosen arbitrarily. Namely, if a perturbation drives the solution to a new pinch point, it will effectively be driven away from the unperturbed solution, which touches down at $x = x_0$.

4.3.3 Unstable Modes

More formally, putting $\bar{\alpha} = (\alpha - 1)/2$, if

$$u(x', t') = t'^{\bar{\alpha}} \bar{U} \left(\frac{x'}{t'^{\beta}} \right)$$

is a similarity solution, then

$$u^{(\Delta)}(x', t') = t'^{\bar{\alpha}} \bar{U} \left(\frac{x' + \Delta}{t'^{\beta}} \right) \equiv t'^{\bar{\alpha}} \bar{U}^{(\Delta)}(\xi, \tau) \quad (4.50)$$

is an equally good solution for any spatial shift Δ . Expanding in Δ we obtain

$$U^{(\Delta)}(\xi, \tau) = \bar{U}(\xi) + \Delta t'^{-\beta} \bar{U}_{\xi} + O(\Delta^2) \equiv \bar{U} + \Delta e^{\beta\tau} \bar{U}_{\xi} + O(\Delta^2). \quad (4.51)$$

But comparing to (4.45), the term linear in Δ must be a solution of (4.46) with eigenvalue $\nu = \beta$ (which for $i = 0$ is $\beta = \alpha + 1 = 3/2$) and eigenfunction $P(\xi) = \bar{U}_{\xi}$. In other words, the unstable mode \bar{U}_{ξ} comes from the fact that a perturbation (of say, amplitude ϵ) to a similarity solution also leads to a shift $x_0(\epsilon)$. If x_0 is not adjusted accordingly, no blow-up will occur at x_0 , which can only mean that one is driven away from the singular solution, which blows up at $x_0(\epsilon)$.

A very similar argument pertains to a shift in t_0 , the time of the singularity. Thus

$$u^{(\Delta t)}(x', t') = (t' + \Delta)^{\bar{\alpha}} \bar{U} \left(\frac{x'}{(t' + \Delta)^{\beta}} \right) \equiv t'^{\bar{\alpha}} \bar{U}^{(\Delta t)}(\xi, \tau).$$

Linearizing for small Δ we obtain

$$\bar{U}^{(\Delta t)}(\xi, \tau) = \Delta e^{\tau} (\bar{\alpha} \bar{U} - \beta \xi \bar{U}_{\xi}),$$

so the time translational eigenvalue is $\nu = 1$, with eigenfunction $\bar{\alpha} \bar{U} - \beta \xi \bar{U}_{\xi}$. This accounts for the next positive exponent in the sequence, but there is also a vanishing eigenvalue (neutral). This comes from the fact that $\xi = -\bar{U} - C \bar{U}^3$ is a continuous family of similarity solutions, which defines

$$u^{(C)} = t'^{\bar{\alpha}} \bar{U}^{(C)}.$$

An expansion in C yields

$$U^{(C)}(\xi, \tau) = \bar{U}^{(\bar{C})}(\xi) + (C - \bar{C}) \frac{\partial \bar{U}}{\partial C},$$

$(C - \bar{C}) \equiv \delta C = \delta C e^{0\tau}$, and so $\nu = 0$ with eigenfunction $P(\xi) = \frac{\partial \bar{U}}{\partial C}$, which is

$$\frac{\partial \bar{U}}{\partial C} = -\frac{\partial \bar{U}}{\partial \xi} \frac{\partial \xi}{\partial C} = -(\xi_{\bar{U}})^{-1}(-\bar{U}^3) = \frac{\bar{U}^3}{1 + 3C\bar{U}^2}.$$

Thus the eigenfunction to the eigenvalue $\nu = 0$ is in parametric form

$$P(-U - CU^3) = \frac{U^3}{1 + 3CU^2}. \quad (4.52)$$

In summary, from the sequence of eigenvalues for $i = 0$, all eigenvalues relevant for the stability of the solution are negative: the solution is stable! The next similarity solution has $i = 1$, and so the sequence of eigenvalues is $\nu = (5 - j)/4$, where $j = 0, 1, 3, 5, \dots$, so that $\nu = 5/4, 1, 1/2, 0, -1, \dots$. The first two eigenvalues are accounted for by the spatial and temporal invariance, respectively. However, apart from the neutral eigenvalue, a positive eigenvalue $\nu = 1/2$ remains. Thus the next higher solution is unstable! This is a situation encountered quite frequently (pinch-off of a fluid thread etc.): only the base solution is stable, all “higher order” solutions are linearly unstable.

4.3.4 The Thin Film Equation

We will return to optics when we study caustics in higher dimensions. But next we will apply the *dynamical systems* formulation to look at the stability of similarity solutions to the thin film equations! Comparing to (4.14) we obtain the dynamical system for the thin film equation:

$$H_\tau = \alpha H - \beta \xi H_\xi - [H^n H_{\xi\xi\xi} + H^{n-m-1} H_\xi]_\xi, \quad (4.53)$$

where $h(x, t) = t'^\alpha H(\xi, \tau)$. Once more we require that $h(x, t)$ be time-independent at constant x' as $t' \rightarrow 0$. Since

$$\frac{dh}{dt'} = t'^{\alpha-1} [\alpha H - \beta \xi H_\xi - H_\tau],$$

this leads to the condition (Eggers & Fontelos, 2015; Witelski & Bernoff, 2000)

$$H_\tau \sim \alpha H - \beta \xi H_\xi, \quad \text{as } |\xi| \rightarrow \infty. \quad (4.54)$$

The dynamical system (4.53) is equivalent to the original equation (4.9), but any similarity solution is a fixed point.

We can now investigate the stability of the sequence of solutions $H_i(\xi)$, that typically exists for any n, m . To this end we put:

$$H(\xi, \tau) = H_i(\xi) + \delta e^{\nu\tau} P(\xi), \quad (4.55)$$

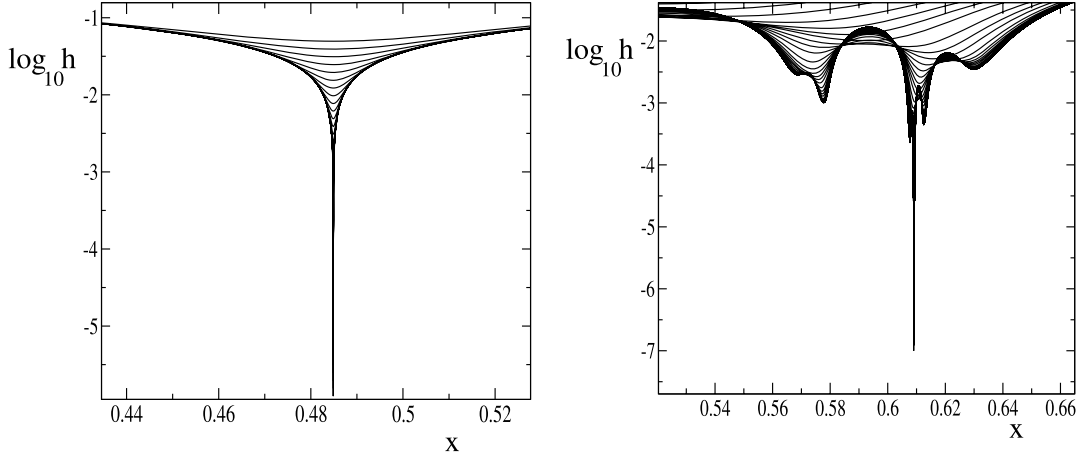


Fig. 4.12 Simulations of (4.8) with $n = 3, m = 2$ (left, regular case), and $n = 3, m = 1.3$ (right, irregular case), plotting $\log_{10} h(x, t)$ as the singularity is approached. Only the neighborhood of the singularity is shown, and a new profile is recorded each time the minimum thickness h_{\min} has decreased by a factor of 0.8

and linearize in δ . This gives the eigenvalue problem

$$\nu P = \alpha P - \beta \xi P_\xi - \left[H_i^n P_{\xi\xi\xi} + n H_i^{n-1} H_{i,\xi\xi\xi} P + H_i^{n-m-1} P_\xi + (n-m-1) H_i^{n-m-2} H_{i,\xi} P \right]_\xi, \quad \nu = \nu_R + \nu_I, \quad (4.56)$$

with the far-field condition $\nu P \approx \alpha P - \beta \xi P_\xi$ for $|\xi| \rightarrow \infty$. Since the eigenvalue problem (4.56) is real, the eigenvalues appear in conjugate pairs.

We solve the eigenvalue problem (see Dallaston et al., 2021a), by either

1. solving a system of ODE's for both the base profile and P , or
2. discretising the eigenvalue equation in ξ ($H_i(\xi)$ given) and solving the resulting algebraic eigenvalue problem to find the eigenvalues.

One technical problem that is always encountered is the existence of unstable directions associated with the invariance in space and time. They need to be identified and the corresponding eigenmodes discarded.

For each point in the (n, m) -plane one finds a semi-infinite sequence of base solutions $H_i(\xi)$, whose stability can be investigated numerically. For example, for $n = 3, m = 2$, for which the similarity profile was shown earlier on the left of Fig. 4.7, $H_0(\xi)$ is stable, all other solutions in the sequence are unstable. This is illustrated by a dynamical simulation of the thin film equation for the corresponding parameter values, as seen on the left of Fig. 4.12. Pinch-off proceeds in a sequence of profiles, whose shape remains the same. Rescaling the x -axis with t^β and the h -axis with t^α results in a collapse on the similarity profile. None of the other similarity solutions are observed.

As we have seen in Fig. 4.7, there are stable fixed points corresponding to both symmetric and asymmetric profiles, e.g. $n = 1.5, m = 0.2$ for an asymmetric profile. An important feature of these fixed points is that the most “dangerous” eigenvalues

($\nu_R < 0$ closest to zero) are complex ($\nu_I \neq 0$). This means that the approach to the self-similar solution is *oscillatory*. For example in viscously dominated pinch-off all eigenvalues are *real*, as can be shown analytically (Eggers, 2012). However, as inertia becomes important (inertial-viscous-surface tension balance) eigenvalues become complex. This has been flagged as the reason for non-uniform or oscillatory approach to the similarity solutions (Dallaston et al., 2021b).

4.3.5 Instability

An exciting discovery came when Dallaston et al. (2017) lowered m below 2 at constant $n = 3$, effectively making the interaction more long-ranged (since h^{-m} decays more slowly away from the minimum). This is illustrated on the right of Fig. 4.12 for $m = 1.3$, for which the profile near a local minimum develops a spatial “instability”. While in the purely self-similar case the solution proceeds with the same shape on smaller and smaller scales, now the solution develops side branches, along which the solution again proceed in a seemingly self-similar fashion, until the side branch becomes once more unstable, and the process repeats itself.

The origin of these instabilities is revealed in Fig. 4.13, where the first two solution branches (the stable ground state solution H_0 , and the first unstable solution H_1) are traced back from $m = 3$ toward smaller values. Each similarity solution is parameterized by its minimum value H_{\min} . Two things are observed:

1. as m decreases, the first two solution branches merge at a fold bifurcation.
2. H_0 (previously stable) becomes unstable at two different Hopf bifurcations.

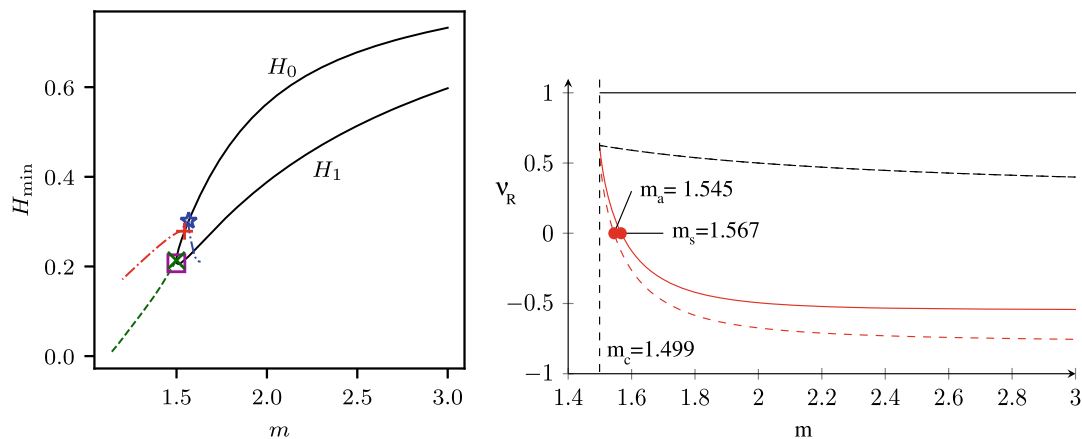


Fig. 4.13 Left: Solution branches for $n = 3$, represented by the minimum value H_{\min} of the similarity profile, as a function of m . Branches H_0 and H_1 are joined at a fold bifurcation. Periodic branches are born at the symmetric and antisymmetric Hopf bifurcations, an unstable asymmetric branch originates from a pitchfork bifurcation. Right: The real part of eigenvalues governing the stability of the primary branch. The imaginary eigenvalues at the Hopf bifurcation are $\nu = \pm 0.912i$ and $\nu = \pm 0.885i$, respectively

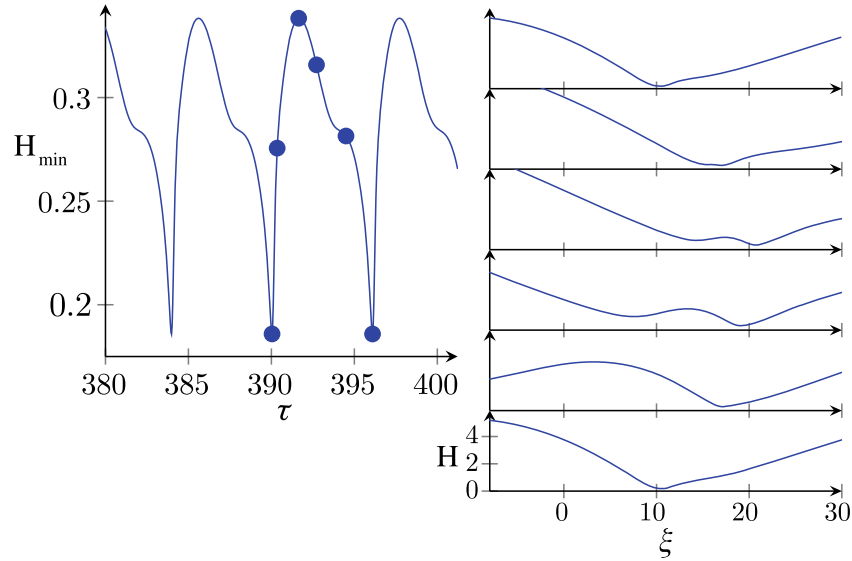


Fig. 4.14 Periodic solutions of (4.53), for $n = 3$ and $m = 1.5$. On the left, H_{\min} as a function of time, on the right, the (asymmetric) profile at the times indicated by the dots. The last profile is identical to the first, as we have completed an entire period

Thus as H_0 is a stable branch and H_1 unstable, the two branches meet at a fold bifurcation. More importantly, as m is lowered along the H_0 -branch, one encounters a Hopf bifurcation (see the right of Fig. 4.13), first at $m_s = 1.567$ against symmetric modes of instability, and then $m_a = 1.545$ against asymmetric modes.

A Hopf bifurcation implies that the real part of the eigenvalue goes through zero at a *finite* imaginary value. At the symmetric and asymmetric Hopf bifurcations, $\nu = \pm 0.912i$ and $\nu = \pm 0.885i$, respectively. This means that the original self-similar solution gives way to something *time-dependent*. At the transition we have

$$H(\xi, \tau) = H_0(\xi) + \delta e^{i\nu_1\tau} P(\xi), \quad (4.57)$$

with period $T = 2\pi/\nu_1$. Thus at a Hopf bifurcation, a new time-dependent solution is born, varying sinusoidally, at a finite frequency. At each of the bifurcations, a new solution branch originates, corresponding to a periodic orbit (of period T close to the value at bifurcation), no longer exactly “circular”. This introduces a new type of solution, no longer self-similar, known as “discrete self-similarity”.

The reason is that the solution varies continuously along a closed curve in function space, with a period T . Only at discrete times $\tau_n = nT + \tau_0$, or $t_0 - t_n = e^{-nT} e^{\tau_0}$, does the solution return to its same rescaled shape $H(\xi, \tau_n)$, hence the name. As is seen in the bifurcation diagram, for $m < m_a$ the profile is asymmetric in space (see the red dot-dashed curve). To trace the time dependence at a value of m slightly below the asymmetric Hopf bifurcation, on the left of Fig. 4.14 we trace the minimum of the similarity profile as a function of τ , which is seen to be periodic. Each point along the curve of course corresponds to an entire profile, whose shapes repeat themselves, as seen on the right for a representative sequence of times, shown as dots on the left.

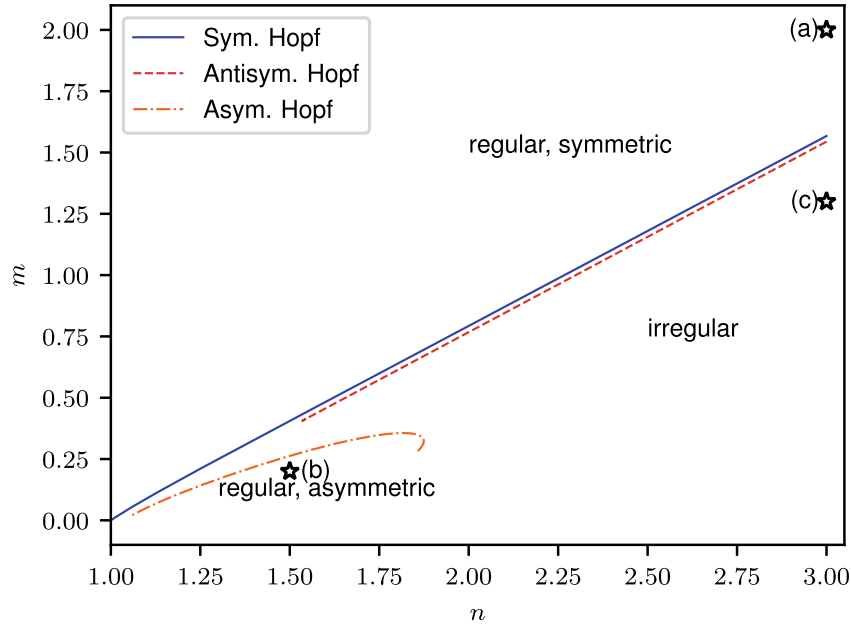


Fig. 4.15 Phase diagram of one-dimensional singular solutions of (4.9). Below the symmetric Hopf bifurcation (solid blue line), regular rupture solutions become unstable, and periodic, or even more complex dynamics appears. A second antisymmetric bifurcation occurs just below (red dashed line). For small values of n below ≈ 1.87 , regular, asymmetric solutions are seen below a Hopf bifurcation in the reverse direction (orange dot-dashed line)

Notice that although H_0 first becomes unstable to a symmetric Hopf bifurcation, the time-dependent solution observed for small m is actually the asymmetric branch, as seen in Fig. 4.14.

Above we have described the transition toward periodic motion for $n = 3$; this transition can now be tracked systematically as a function of n , as shown in Fig. 4.15. The full phase diagram is more complicated, but to a good approximation regular motion is observed for

$$m > 0.8(n - 1) : \text{ regular dynamics.} \quad (4.58)$$

Finally, it is observe that for even smaller m , the solution no longer appears to be periodic, but orbits are more complicated. The complexity of spatial patterns suggest *chaotic* behavior, always generating new profiles.

4.3.6 Drop Pinching

Irregular behavior has been observed in many systems. A particularly interesting example is viscous breakup of one fluid in another, in the limit that the inner fluid viscosity is much smaller: $\lambda = \eta_{in}/\eta_{out}$, $\lambda \ll 1$. As seen in Fig. 4.16, several sequences of instability, closely resembling discrete self-similarity, are observed in an exper-

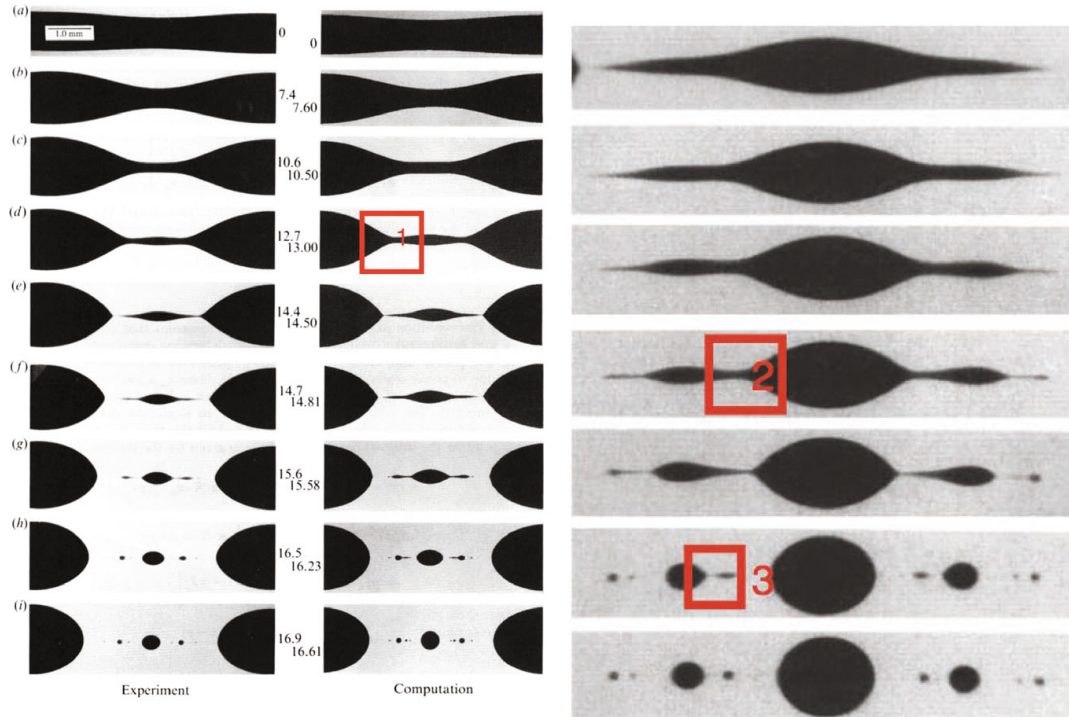


Fig. 4.16 The breakup of a fluid filament, whose viscosity is smaller by a factor 0.067 relative to the surrounding fluid (Tjahjadi et al., 1992). On the left, the overall dynamics are compared between theory and experiment; on the right, a blowup of the last stages of the experiment is seen. The same sequence of events repeats itself several times, and three stages of the same event are numbered 1–3

iment (far left), and are reproduced in the corresponding panel immediately to the right, showing a numerical simulation. Each detail of the experiment is indeed reproduced by a simulation of Stokes' equation. The blow-up of the experimental sequence on the far right shows three stages of the same sequence.

Starting from Stokes' equation, using the approximation of a slender filament, the problem has been re-examined theoretically by Fontelos and Wang (2021). After some rescaling (which eliminates λ), the slender equations can be written in the form

$$\frac{\partial h}{\partial t} = ph - 1, \quad p = \frac{1}{h} + \frac{1}{h^2} (h^4 p')'.$$

They are simple enough so they can be studied in detail; an analysis of the dynamical system in self-similar variables indeed shows periodic behavior (discrete self-similarity). There are indications that the time dependence might even be more of a more complicated, non-periodic form.

4.4 Multidimensional Singularities

So far we have only looked for solutions in one dimension, but in general singularities develop in arbitrary dimensions. A general ansatz is

$$h(x, y, t) = t'^{\alpha} H(\xi, \eta), \quad \xi = \frac{x'}{t'^{\beta}}, \quad \eta = \frac{y'}{t'^{\bar{\beta}}}, \quad (4.59)$$

where x' and y' are the distances to the location of the singularity, at x_0, y_0 . We assume that the equation of motion itself does not favor a particular spatial direction. We will see that two cases arise:

1. $\beta = \bar{\beta}$: “pointlike” singularity, for example when the singularity is radially symmetric
2. $\bar{\beta} = 1/2$: “quasi-one-dimensional”, consistent if the variation in the transversal direction is slow, namely $\beta > \bar{\beta} = 1/2$.

Apart from systems examined in more detail below, examples of these two types of multi-dimensional singularities have recently been observed in drop coalescence. Pointlike singularities have been seen in liquid lenses (drops floating on another liquid) (Klopp et al., 2020) and quasi-one-dimensional singularities in sessile drops on a solid substrate (Kaneelil et al., 2022).

In the following, we assume that the coordinate system has been adjusted so that the direction in which gradients are greatest is the x -direction. Since the variation in the y -direction is slow, we can look at the solution as a superposition of one-dimensional solutions, as a parameter is varied. Since $\nu_T = 1$ is usually the most singular eigenvalue, this is effectively the singularity time $t_c(y)$. Let us choose the origin of y such that a singularity occurs for $y = 0$ first.

Expanding, we have $t_c(y) = t_0 + Ay^2 + O(y^3)$, where A must be a positive number, otherwise t_0 would not be the time of the earliest singularity; for the same reason there is no linear term. Thus effectively for each y we have for the one-dimensional singularity $t_c - t = t' + Ay^2$, which implies $y^2 \sim t'$, and so $\bar{\beta} = 1/2$. Thus we have

$$h(x, y, t) = t'^{\alpha} H\left(\frac{x'}{t'^{\beta}}, \frac{y'}{t'^{1/2}}\right) \equiv t'^{\alpha} H(\xi, \eta), \quad (4.60)$$

which is consistent if $\beta > 1/2$. In that case $h_x = t'^{\alpha-\beta} H_{\xi} \gg h_y = t'^{\alpha-1/2} H_{\eta}$, so that the right hand side of (4.10) becomes to leading order

$$-t'^{\alpha-1} [H^n H_{\xi\xi\xi} + H^{n-m-1} H_{\xi}]_{\xi},$$

and the two-dimensional similarity equation of the thin film problem becomes

$$-\alpha H + \beta \xi H_{\xi} + \frac{\eta}{2} H_{\eta} = -[H^n H_{\xi\xi\xi} + H^{n-m-1} H_{\xi}]_{\xi}. \quad (4.61)$$

This applies for $\beta = \frac{1+m}{4+4m-2n} > 1/2$, or

$$n > 1 + m, \quad \text{quasi-one-dimensional.} \quad (4.62)$$

Now we can, starting from *any* one-dimensional description $H^{(1)}(\xi)$, find the unfolded solution in general dimensions. We find that

$$H(\xi, \eta) = (1 + A\eta^2)^\alpha H^{(1)}\left(\frac{\xi + B\eta^{2\beta}}{(1 + A\eta^2)^\beta}\right) \quad (4.63)$$

is a solution of (4.61) for arbitrary constants A, B , as can be checked by direct substitution. Here we have allowed for a detuning in space as well, to arrive at a more general form of solution. The constants are adjustable parameters, which depend on initial conditions. Note that $\eta^{2\beta}$ is in general a singular contribution unless 2β is an integer, for example when $\beta = 1$. In that case

$$\Delta x = x - x_c = x' - by^2, \quad \frac{\Delta x}{t'^\beta} = \xi - b\frac{y^2}{t'} = \xi - b\eta^2,$$

as required.

The same idea can be applied to the solution of the dynamical system

$$H_\tau = \alpha H - \beta \xi H_\xi - \frac{\eta}{2} H_\eta - \left[H^n \left(H_{\xi\xi} - \frac{1}{m H^m} \right) \right]_\xi; \quad (4.64)$$

now if $H^{(1)}(\xi, \tau)$ is a solution of (4.53),

$$H(\xi, \eta) = (1 + A\eta^2)^\alpha H^{(1)}\left(\frac{\xi + B\eta^{2\beta}}{(1 + A\eta^2)^\beta}, \frac{\tau}{1 + A\eta^2}\right) \quad (4.65)$$

solves (4.64).

Analogous expressions work in arbitrary dimensions, and for all isotropic problems. On the other hand, for $n \leq 1 + m$ (so that $\beta \leq 1/2$), a pointlike singularity is observed. Inserting (4.59) with $\bar{\beta} = \beta$ into the generalized thin film equation (4.10), we obtain the similarity solution

$$-\alpha H + \beta \xi H_\xi + \beta \eta H_\eta = -\nabla \cdot (H^n \nabla \Delta H + H^{n-m-1} \nabla H), \quad (4.66)$$

where $\nabla = (\partial_\xi, \partial_\eta)$, and $\Delta = \partial_\xi^2 + \partial_\eta^2$. In view of spatial isotropy, it is natural to look for solutions of (4.66) which are axisymmetric (Witelski & Bernoff, 2000; Zhang & Lister, 1999). The scaling of the exponents (4.13) is the same as in the one-dimensional case. This leads to the radially symmetric solution

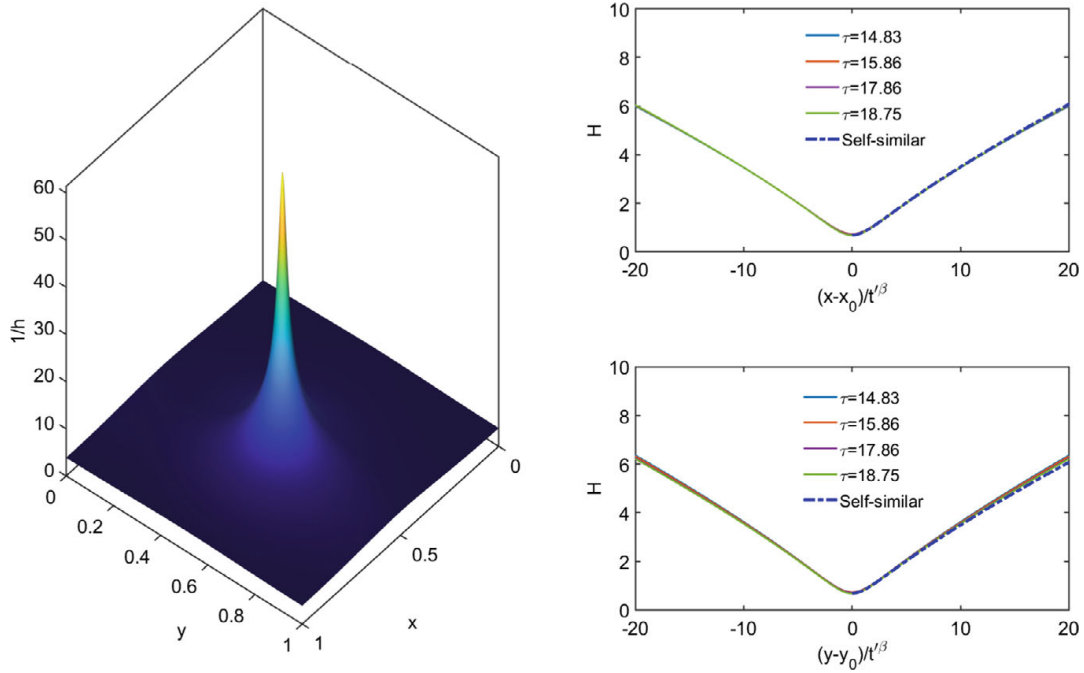


Fig. 4.17 Simulation of (4.10) with $n = 2$, $m = 1.5$, ($\alpha \approx 0.33$, $\beta \approx 0.42$), and initial condition (4.69), using $\epsilon_1 = 0.05$, $\epsilon_2 = 0.03$, and $h_{\text{ref}} = 0.2$. On the left, a perspective plot of $1/h$ at $\tau = 10.1$ demonstrates the pointlike character. On the right, cuts in the x and y directions are shown at the top and bottom, respectively, for the values of $\tau = -\ln t'$ shown. Profiles are collapsed according to (4.67), and agree with a solution of (4.68) (dot-dashed line), demonstrating axisymmetry

$$h(x, y, t) = t'^{\alpha} H(\rho), \quad \rho = r/t'^{\beta}, \quad (4.67)$$

for which the similarity equation becomes in two dimensions:

$$-\alpha H + \beta \rho H_{\rho} + \frac{1}{\rho} \left[\rho H^n \left(\frac{(\rho H_{\rho})_{\rho}}{\rho} \right) + H^{n-m-1} H_{\rho} \right]_{\rho} = 0. \quad (4.68)$$

Let us explore the validity of the two types of solution: quasi-one-dimensional or pointlike. As the initial condition we choose

$$h_0(x, y) = h_{\text{ref}} [1 - \epsilon_1 \cos 2\pi(x - 1/2)] [1 - \epsilon_2 \cos 2\pi(y - 1/2)], \quad (4.69)$$

which helps explore transitions between one and two dimensions. If $\epsilon_2 = 0$, there is no y -dependence, and solutions are strictly one-dimensional. If on the other hand $\epsilon_1 = \epsilon_2$, there is a single minimum at the center $(x, y) = (1/2, 1/2)$ of the domain, around which the profile is approximately axisymmetric. The mean thickness h_{ref} was chosen such that a flat profile is linearly unstable.

The case of Fig. 4.17 is in the pointlike (axisymmetric) regime. According to (4.13), $\beta \approx 0.42 < 1/2$, so a transverse perturbation, resulting in an effective shift

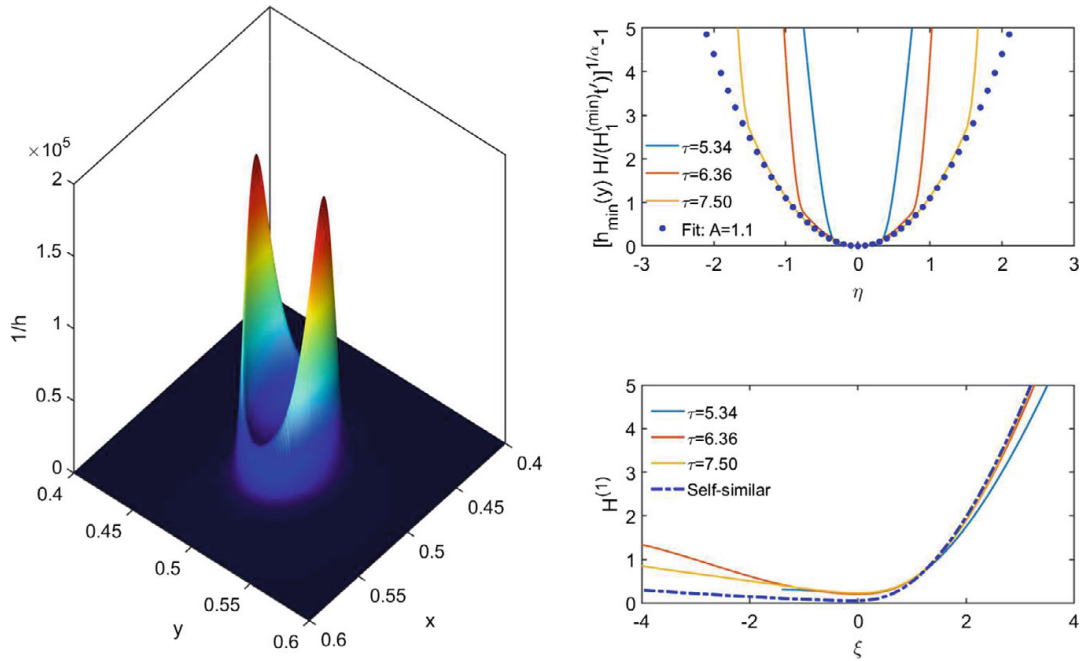


Fig. 4.18 Simulation of (4.10) with $n = 1.7$, $m = 0.2$ ($\alpha \approx 1.42$, $\beta \approx 0.86$), and initial condition (4.69), using $\epsilon_1 = 0.05$, $\epsilon_2 = 0.03$, and $h_{\text{ref}} = 0.04$. A quasi one-dimensional, regular singularity is observed. On the left, a perspective plot of $1/h$ at $\tau = 7.5$ with two quasi one-dimensional peaks; on the bottom right, a collapse of the profiles using (4.59), compared to (4.63). Upper right, transversal collapse using (4.70)

in t_0 , only produces a localized perturbation inside the peak, which remains stable. As seen on the left of Fig. 4.17, although the initial condition is not axisymmetric, the solution converges to a point, with radial symmetry. We show a perspective plot of $1/h$, and emphasize contour lines using a color scale. To demonstrate axisymmetry more clearly, we show collapse of the profiles in the x and y directions on the right. Cuts in both directions are rescaled according to (4.67). In both cases one observes very good collapse, and very good agreement with the solution to the axisymmetric similarity equation (4.68). We find the same pointlike behavior for all of the cases above the blue dashed line.

Next we look at a quasi one-dimensional case, shown in Fig. 4.18. Choosing $n = 1.7$, $m = 0.2$, we look at a case of regular fixed point dynamics, found underneath the dot-dashed orange curve of Fig. 4.15; the one-dimensional profiles are highly asymmetric, as shown in the lower right. On the left of Fig. 4.18, we once more plot $1/h$ over the (x, y) -plane, and indicate contours by color; owing to the symmetry of the initial condition, we now see two equal peaks. The exponent controlling the width of the singularity is $\beta \approx 0.87 > 1/2$, so a transversal perturbation now leads to a growth of one-dimensional singularities over a scale $t^{1/2}$, which is much larger than their width. Indeed, the peaks are seen to be extremely anisotropic: much thinner in the y -direction than they are in the x -direction.

Note that the definition of ξ and η in (4.59) must be read with the roles of x and y reversed. In general, one should apply (4.59) with the x -direction chosen as

the direction of the largest gradient, y in the direction orthogonal to it. Looking at the front and back of the peak, one appreciates the asymmetry of the profile in the y -direction. In the x -direction, on the other hand, the solution is unfolded: the peak is highest along the centerline $x = 0.5$, and with increasing $|x - 0.5|$, one sees the singularity at earlier stages of its evolution.

On the right of Fig. 4.18, the structure of the singularity, as described by (4.63), is analyzed more quantitatively. In the generic case of 2β not being an integer ($2\beta = 1.71$ in the example), we have $B = 0$, and it remains to calculate A . To that end, we calculate the minimum $H_{\min}^{(1)}$ of the one-dimensional similarity profile by solving the one-dimensional similarity equation (4.14). Now we calculate the minimum of h for different values of y . From (4.63) it follows that

$$\left(\frac{h_{\min}(y)}{H_1^{(min)} t'^{\alpha}} \right)^{1/\alpha} - 1 = A\eta^2, \quad (4.70)$$

and so A is found from plotting the left hand side as a function of η . On the upper right of Fig. 4.18, one sees a collapse toward a quadratic profile as τ increases; from a fit to the quadratic profiles we find $A = 1.1$. Now we can test for the collapse of the whole profile using (4.63), as shown on the lower half on the right of Fig. 4.18. Once again, there is a good collapse and agreement with the self-similar solution, shown by the dot-dashed line.

4.5 Pointlike and Quasi-1dimensional Singularities: The Eikonal Equation

4.5.1 Quasi-1dimensional

The difference between pointlike and quasi-one-dim. singularities can be studied in particular detail using the eikonal equation. Let us concentrate on the cusp case, described in Sect. 4.2.5 above in one dimension, which corresponds to $i = 0$, $\alpha = 2$, and $\beta = 3/2 > 1/2$. However, now we look at the two-dimensional version:

$$z = t + |t|^\alpha h(\xi, \eta), \quad \xi = x/|t|^{3/2}, \quad \eta = y/|t|^{1/2},$$

with similarity equation

$$4h - 3\xi h_\xi - \eta h_\eta \pm h_\xi^2 = 0.$$

Differentiating with respect to ξ and putting $U = h_\xi$, we obtain

$$U - 3\xi U_\xi - \eta U_\eta \mp U U_\xi = 0, \quad (4.71)$$

a semilinear equation. Before solving (4.71) directly, we note that the one-dimensional solution $U^{(1)}(\xi)$ satisfies

$$\xi = \mp U^{(1)} - C(U^{(1)})^3,$$

and thus according to (4.63),

$$U(\xi, \eta) = (1 + A\eta^2)^2 U^{(1)} \left(\frac{\xi + B\eta^3}{(1 + A\eta^2)^{3/2}} \right)$$

is a two-dimensional solution. Combining the two equations we obtain

$$\frac{\xi + B\eta^3}{(1 + A\eta^2)^{3/2}} = \mp (1 + A\eta^2)^{1/2} U - C(1 + A\eta^2)^{3/2} U^3,$$

or

$$\xi = \mp (1 + A\eta^2) U - CU^3 - B\eta^3. \quad (4.72)$$

However, in the case of the eikonal equation this is not the most general solution of (4.71). Namely, transforming (4.71) to $\xi(U, \eta)$ we have $U_\eta = -U_\xi \xi_\eta$, $U_\xi = (\xi_U)^{-1}$, and thus

$$\xi_U U - 3\xi + \eta \xi_\eta \pm 2U = 0,$$

with general solution

$$\xi = \mp U - U^3 F \left(\frac{\eta}{U} \right), \quad (4.73)$$

F being an arbitrary function. However, taking the fourth derivative of (4.73) with respect to η , we obtain

$$\frac{\partial^4 \xi}{\partial \eta^4} = -\frac{1}{U} F^{iv} \left(\frac{\eta}{U} \right),$$

which is singular at $U = 0$, unless $F^{iv}(x) = 0$, i.e. F must be a polynomial of third degree: $F(x) = A_0 + A_1x + A_2x^2 + A_3x^3$. Thus we finally obtain

$$\xi = \mp U - A_0U^3 - A_1U^2\eta - A_2U\eta^2 - A_3\eta^3, \quad (4.74)$$

which is consistent with, but more general, than (4.72), which only contains three constants, instead of the four constants contained in (4.74). Integrating, we obtain a general solution for a wave front in two dimensions:

$$h = \mp \frac{U^2}{2} - \frac{3A_0}{4}U^4 - \frac{2A_1}{3}U^3\eta - \frac{A_2}{4}U^2\eta^2 + \bar{f}(\eta). \quad (4.75)$$

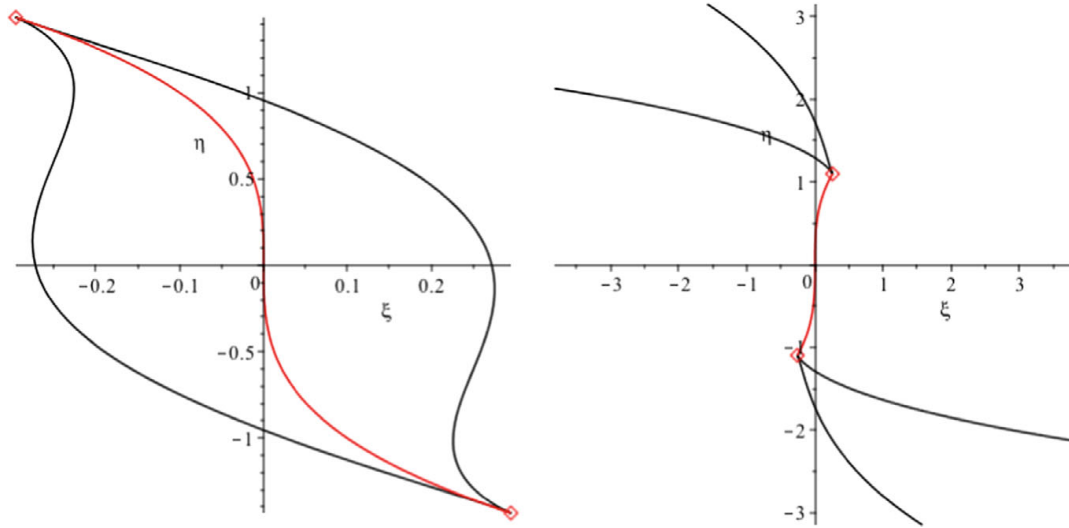


Fig. 4.19 A lips event with parameters $A_0 = 2$, $A_1 = 0.3$, $A_2 = 0.5$, and $A_3 = 0.1$ (left), and a beak-to-beak event with $A_0 = 1$, $A_1 = 25$, $A_2 = 0.5$, and $A_3 = 0.1$ (right), as described by (4.76), (4.77). The red line, described by the first equation of (4.80), is the cusp of the caustic surface, projected onto the ξ, η -plane. It ends at the position marked by the diamonds

As we can formally parameterize ξ and η by (U, η) , and since $\eta_\eta = 1$, $\eta_U = 0$, the caustic condition (4.31) is again $0 = \xi_U \eta_\eta - \xi_\eta \eta_U = \xi_U$. Using the lower sign of (4.74) (so that a caustic has formed), we find

$$1 = 3A_0U^2 + 2A_1U\eta + A_2\eta^2, \quad (4.76)$$

which defines a curve in the (U, η) -plane, which we can parameterize. Inserting into (4.74), we find

$$\xi = 2A_0U^3 + A_1U^2\eta - A_3\eta^3, \quad (4.77)$$

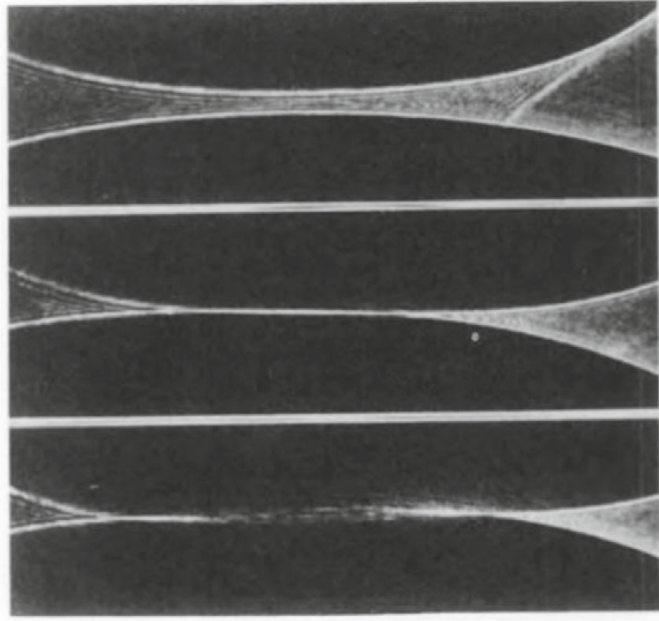
so that (4.76) together with (4.77) defines a curve in the (ξ, η) -plane, as shown in Fig. 4.19. Two cases arise: if the quadratic form (4.76) is positive definite,

$$A_0 > 0, \quad D = 3A_0A_2 - A_1^2 > 0, \quad (4.78)$$

(4.76) can only be satisfied if $t > 0$ (corresponding to the lower sign shown). In this case (4.76) defines an ellipse, and we obtain a closed curve, as shown on the left of Fig. 4.19. If on the other hand the quadratic form is negative definite ($D < 0$ in (4.78)), we will produce two pieces, as shown on the right.

A typical experiment is shown in Fig. 4.20, where one sees different planes perpendicular to the direction z of propagation. As one travels in the direction of observation (going from top to bottom), a closed curve separates into two. This is known as a beak-to-beak event. To interpret this result, we look at the evolution as a function of time in real space. We have (always for $t > 0$) $y = t^{1/2}\eta$ and $u = t^{1/2}U$, so that (4.76) is

Fig. 4.20 A beak-to-beak event, as described theoretically by (4.79), and shown on the right of Fig. 4.19. Horizontal cuts through the surface shown on the right of Fig. 4.21 explain the transition from a single piece to two separate curves



$$z = t = 3A_0u^2 + 2A_1uy + A_2y^2,$$

which together with (4.77) defines the caustic surface: all places swept out by the singularities of the wave front as it propagates in space. To write the result in similarity variables, we introduce Z as a rescaled distance in the propagation direction: $z = Zt$, so that

$$Z = 3A_0U^2 + 2A_1U\eta + A_2\eta^2, \quad \xi = 2A_0U^3 + A_1U^2\eta - A_3\eta^3 \quad (4.79)$$

defines the caustic surface in similarity variables.

Two examples of such a surface are shown in Fig. 4.21, the case $D > 0$ being shown on the left, $D < 0$ on the right. If one considers a cut through either surface at constant $\eta = 0$, one recovers the one-dimensional coffee-cup cusp shown experimentally in Fig. 4.10 or theoretically on the right of Fig. 4.11. As η is varied, the surfaces end in a line of cusps, shown as the red lines. Indeed, it follows from (4.79) that $\xi_U = UZ_U$, so the condition $\xi_U = 0$ implies $Z_U = 0$ as well, so that $\xi_U = 0$ defines the cusp of the caustic surface as $U = A_1\eta/(3A_0)$. Plugging this back into (4.79), the cusp line is parameterized as

$$\xi_c = \left(\frac{A_1^3}{27A_0^2} - A_3 \right) \eta^3, \quad Z_c = \frac{D}{3A_0} \eta^2. \quad (4.80)$$

The space curve defined by (4.80) is shown as the red lines in Fig. 4.21.

This means that for $D < 0$ the cusp line is bent downwards (see the right surface of Fig. 4.21), and the caustic singularities appear first as two different pieces, and

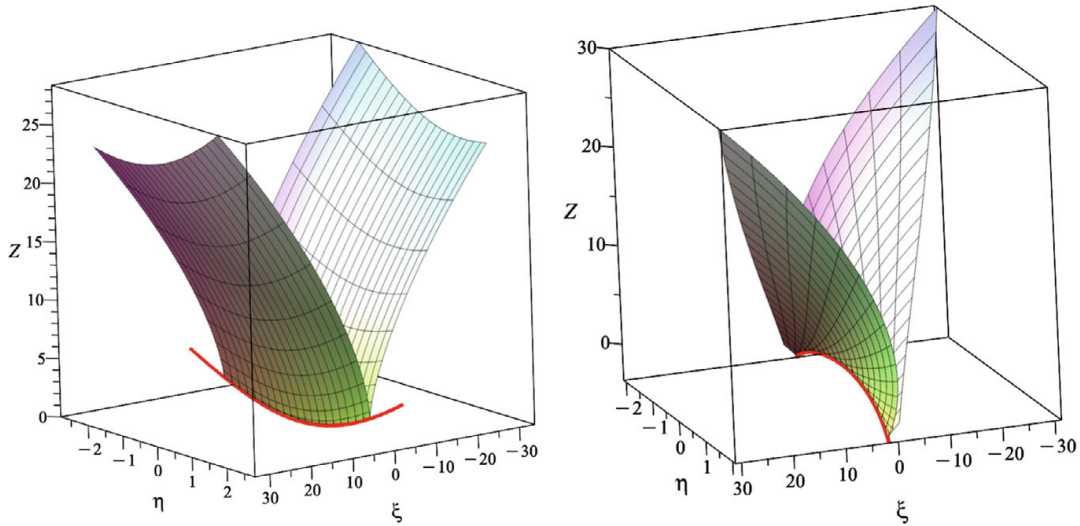


Fig. 4.21 Caustic surfaces in the case of lips (left) and beak-to-beak events (right), as computed from (4.79); parameters are the same as in Fig. 4.19. On the left, $D > 0$ and the cusp line (red) curves upwards, on the right $D < 0$ and the cusp line curves downwards

are joined together when the plane of observation is raised above the maximum of (4.80): this is what we introduced earlier as a beak-to-beak event, and the sequence is shown in Fig. 4.20 going from the bottom to the top. If on the other hand $D > 0$ (left of Fig. 4.21), the singularity first occurs at a point in the center, and then expands to a figure as shown on the left of Fig. 4.19; this is called a “lips” event. The cusp line, projected onto the (ξ, η) -plane, is shown as the red lines in Fig. 4.19 for both cases.

Catastrophe theory As an aside, it should be mentioned that there exists a highly developed theory, known as catastrophe theory, which classifies optical singularities. In doing so, it makes use of the fact that the evolution of a wave front can be written as a smooth mapping, as can be seen by (4.23) in Sect. 4.2.4 above. The singularities of such mappings can be classified completely, and allow the description of much more complicated sequences than those shown above. In particular, the caustics need not be described by a single set of similarity exponents, but the different parts of the picture can scale in different ways.

However, the classification is valid only up to smooth deformations, which allows the picture to be “straightened out”, without there being a systematic way to reconstruct the original image. For example, in Nye (1999), the caustic surface for the cusp is reported in the form

$$\xi^2 = (Z - \beta\eta^2)^3, \quad (4.81)$$

using the same notation as in (4.79). The form (4.81) results from deforming the cusp line to lowest, quadratic order. However, (4.81) fails to represent the most general form (4.79) of the caustic surface. Only in the particular case $A_0 = A_3 = 0$ does (4.79) reduce to

$$\xi^2 = \frac{2A_0}{27A_0^3}(Z - A_2\eta^2)^3,$$

which up to a trivial rescaling is equivalent to (4.81).

However, if one is able to disentangle what the smooth transformations were, which lead to a simplified version such as (4.81), then one should be able to reconstruct the structure in full generality. This was achieved by J. Hannay, who found a generalization of (4.81), which is equivalent to (4.76) and (4.74), yet much simpler:

$$\xi = a\eta^3 + b\eta \pm \alpha \left(1 - \frac{\eta^2}{\eta_c^2}\right)^{3/2}. \quad (4.82)$$

The coefficient α is found by comparing the value of $\xi(\eta = 0)$: $\alpha = 2A_0/(3A_0)^{3/2}$; the values of a and b are found from the position (ξ_c, η_c) of the cusp, and the slope of the cusp tangent:

$$a = \frac{9A_0A_1A_2 - 27A_0^2A_3 - A_1^3}{27A_0^2}, \quad b = -\frac{A_1}{3A_0}. \quad (4.83)$$

4.5.2 Pointlike Singularities

Since $\beta > 1/2$, the quasi-one-dimensional case described above is the generic one. However, initial conditions can be found to achieve any kind of singularity, if one allows to adjust a sufficient number of parameters. In that way one can achieve the case $\beta = \bar{\beta} = 3/2$, which we discuss now. It is of codimension 1 (Nye, 1999), which means a single parameter needs to be adjusted to achieve it. For isotropic singularities $\beta = \bar{\beta}$ we have solutions of the form

$$z = t + |t|^\alpha h(\xi, \eta), \quad \xi = \frac{x}{|t'|^{(\alpha+1)/2}}, \quad \eta = \frac{y}{|t'|^{(\alpha+1)/2}}, \quad (4.84)$$

which yields the similarity equation

$$2\alpha h - (\alpha + 1)(\xi h_\xi + \eta h_\eta) \pm h_\xi^2 + h_\eta^2 = 0. \quad (4.85)$$

This is a fully nonlinear first order equation, harder to solve than the semi-linear cases encountered so far.

In principle, axisymmetric solutions are possible:

$$z = t + |t|^\alpha h(\rho), \quad \rho = \frac{r}{|t'|^{(\alpha+1)/2}},$$

and so

$$2\alpha h - (\alpha + 1)\rho h_\rho \pm h_\rho^2 = 0.$$

However, this corresponds to a very special initial condition, in which all rays focus on exactly one point: a highly non-generic situation. Therefore, we look for general solutions of (4.85), which need not be axisymmetric. The equation is now fully non-linear, so its solution is non-trivial; it can however be found using Charpit's method (Ockendon et al., 2003). In the paragraph below, we will explain a more intuitive procedure using Fermat's principle. The result is

$$\begin{aligned} h &= \pm 2(\Phi^2 + \Psi^2) - \Phi^{\frac{2\alpha}{\alpha-1}} F\left(\frac{\Psi}{\Phi}\right), \quad \xi = \frac{\alpha-1}{2\alpha+2} h_\Phi \pm \frac{4}{\alpha+1} \Phi, \\ \eta &= \frac{\alpha-1}{2\alpha+2} h_\Psi \pm \frac{4}{\alpha+1} \Psi, \end{aligned} \quad (4.86)$$

with $F(x)$ an arbitrary function. Once more, for h to be regular, the exponent $2\alpha/(\alpha-1)$ must be an integer $i = 3, 4, \dots$; then the similarity exponents are $\alpha = i/(i-2)$, $\beta = (i-1)/(i-2)$. In the simplest case $i = 3$ (so that $\alpha = 3, \beta = 2$, the so-called umbilic catastrophe), the similarity solution is

$$h = \pm 2(\Phi^2 + \Psi^2) - \Phi^3 F\left(\frac{\Psi}{\Phi}\right), \quad \xi = \frac{h_\Phi}{4} \pm \Phi, \quad \eta = \frac{h_\Psi}{4} \pm \Psi; \quad (4.87)$$

again, taking derivatives of h with respect to Ψ we see that h becomes singular unless F is a polynomial of degree 3: $F(x) = A_0 + A_1x + A_2x^2 + A_3x^3$.

The caustic condition (4.31) is now

$$\xi_\Phi \eta_\Psi - \xi_\Psi \eta_\Phi = 0; \quad (4.88)$$

the case $i = 3$ has codimension 1: another parameter (apart from time) has to be adjusted to find it. Using the polynomial form of F , the wave front becomes

$$\begin{aligned} h &= \pm 2(\Phi^2 + \Psi^2) + A_0\Phi^3 + A_1\Psi\Phi^2 + A_2\Psi^2\Phi + A_3\Psi^3, \\ \xi &= \pm 2\Phi + 3A_0\Phi^2/4 + A_1\Psi\Phi/2 + A_2\Psi^2/4, \\ \eta &= \pm 2\Psi + 3A_3\Phi^2/4 + A_2\Psi\Phi/2 + A_1\Psi^2/4, \end{aligned} \quad (4.89)$$

and the caustic condition (4.88) is

$$\begin{aligned} 0 &= c_{11}\Phi^2 + 2c_{12}\Phi\Psi + c_{22}\Psi^2 \pm 2c_1\Phi \pm 2c_2\Psi + D_0 \equiv \quad (4.90) \\ &\frac{3A_0A_2 - A_1^2}{4}\Phi^2 + \frac{9A_0A_3 - A_1A_2}{4}\Phi\Psi + \\ &\frac{3A_1A_3 - A_2^2}{4}\Psi^2 \pm (3A_0 + A_2)\Phi \pm (3A_3 + A_1)\Psi + 4. \end{aligned}$$

Note that the two different signs just lead to an opposite sign of Φ, Ψ , and so ξ and η remain the same both before and after the singularity. The condition (4.90), together with (4.89), again leads to a curve in the (ξ, η) -plane, which is shown in

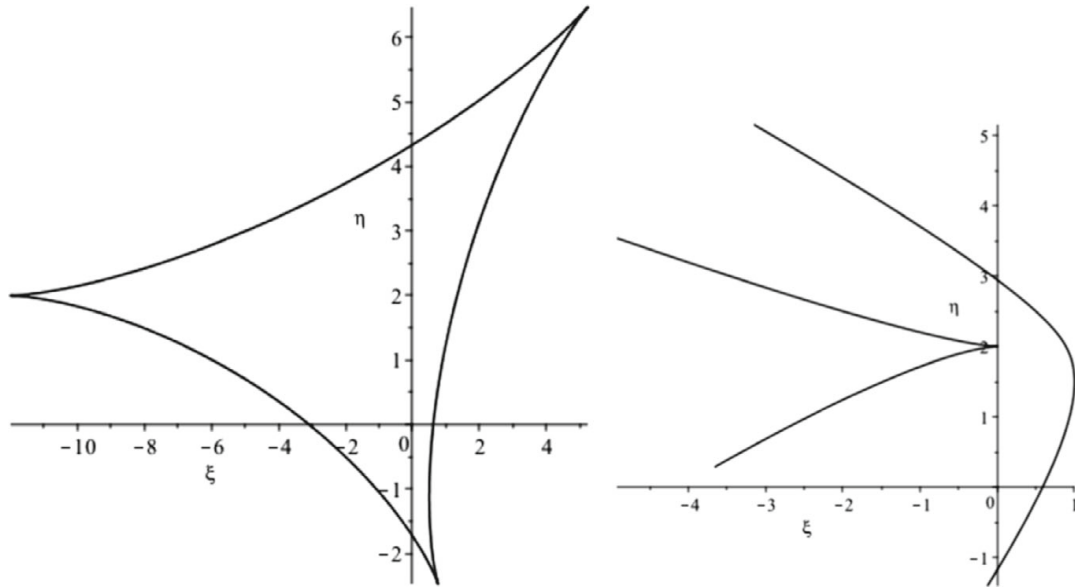


Fig. 4.22 The elliptic umbilic (left) and hyperbolic umbilic (right) caustics according to (4.89) with constraint (4.90)

Fig. 4.22. There are two types, depending on the sign of

$$D = c_{11}c_{22} - c_{12}^2; \quad (4.91)$$

The case $D > 0$ is called the elliptic umbilic, shown on the left, while $D < 0$ is called the hyperbolic umbilic, shown on the right of Fig. 4.22. For a proper description of the singular case $D = 0$ one needs to consider higher order terms, which break scale invariance. To obtain the figure, we parameterize (4.90) by writing it as a quadratic form in the variables $\bar{\Phi} = \Phi - \Phi_s$ and $\bar{\Psi} = \Psi - \Psi_s$, and then insert it into (4.89) to obtain a curve in the (ξ, η) -plane.

Experimental images such as Fig. 4.23 can once more be interpreted as cuts through a caustic surface at different levels Z in the propagation direction. Such a caustic surface is obtained in the same way as before, giving

$$\begin{aligned} \xi &= -2Z\Phi + 3A_0\Phi^2/4 + A_1\Psi\Phi/2 + A_2\Psi^2/4, \\ \eta &= -2Z\Psi + 3A_3\Phi^2/4 + A_2\Psi\Phi/2 + A_1\Psi^2/4, \\ 0 &= c_{11}\Phi^2 + 2c_{12}\Phi\Psi + c_{22}\Psi^2 - 2c_1Z\Phi - 2c_2Z\Psi + D_0Z^2, \end{aligned} \quad (4.92)$$

where $z = |t|Z$ as usual. An example is shown in Fig. 4.24, and seen to correspond well to the top of Fig. 4.23. The hyperbolic umbilic at the bottom of Fig. 4.23, on the other hand, corresponds well to the theoretical prediction on the right of Fig. 4.22.

Similarity solutions via Fermat's principle Here we show how to derive similarity solutions using Fermat's principle, having the advantage of using a single scalar function ℓ , as defined by (4.24). We focus on the "isotropic" solutions of Sect. 4.5.2,

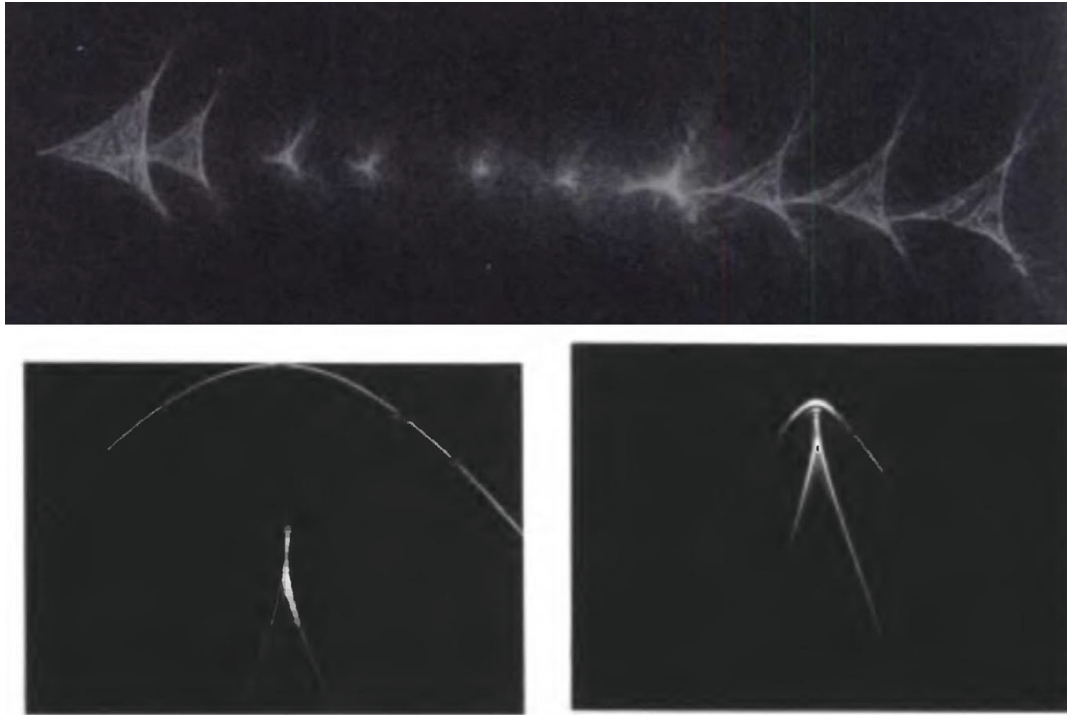
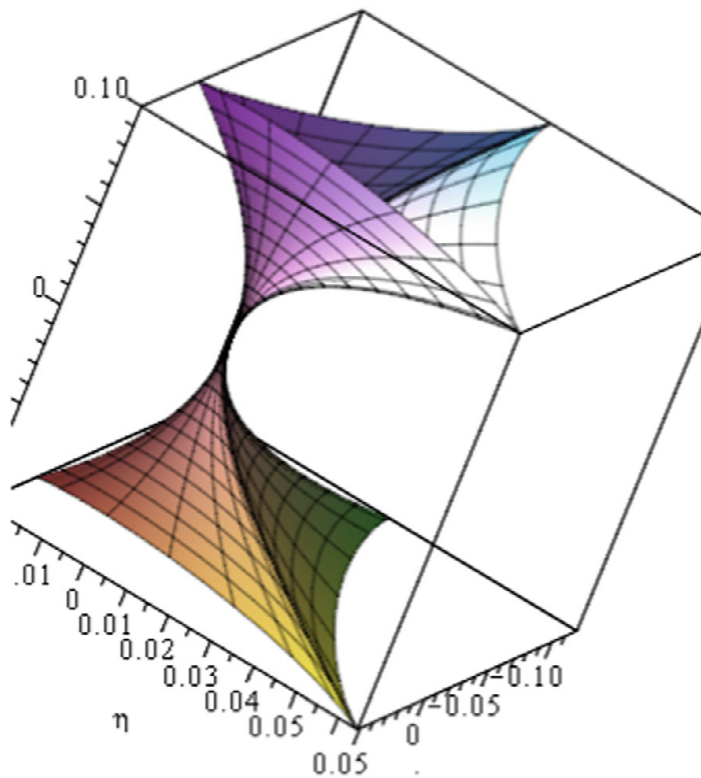


Fig. 4.23 Experimental realizations of the caustics seen in Fig. 4.22. Top: Elliptic umbilic; Bottom: Hyperbolic umbilic

Fig. 4.24 The elliptic umbilic surface, as described by (4.92)



since they are difficult to find directly from the similarity equation (4.85), which is fully non-linear but the quasi-one-dimensional solutions can be found in the same way. The idea is to start from the perfectly focusing solution (i.e. a circular wave front) and to add a perturbation. Let the initial condition be parameterized in two dimensions by $\mathbf{u} \equiv (\varphi, \psi)$. Let us consider a circle of radius 1 at time $t = -1$, so that a perfect focus is produced at the axis $x = y = 0, z = 1$, at $t = 0$:

$$f = 1 - \sqrt{1 - \varphi^2 - \psi^2}, \quad t = -1.$$

We focus on the umbilic case $i = 3$, but the procedure can be generalized.

Based on the similarity solution, we have

$$x = t^2 \xi, \quad y = t^2 \eta, \quad z = 1 + t + t^3 h,$$

where the additive constant ensures $z = 1$ for $t = 0$; this is valid for $t > 0$. Focusing takes place at $t = 1$. Corresponding to the scaling with t^3 , we choose the perturbation

$$f = 1 - \sqrt{1 - \varphi^2 - \psi^2} + \varphi^3 G(\psi/\varphi). \quad (4.93)$$

To ensure $t^3 \sim \varphi^3$, we put $\varphi = t\Phi$ and $\psi = t\Psi$, so that $G = G(\Psi/\Phi)$.

To account for the initial condition being for $t = -1$, we want to solve ($\ell = ct$)

$$\ell_2 \equiv \ell^2 - (1 + t)^2 = 0,$$

where

$$\ell^2 = (x - \varphi)^2 + (y - \psi)^2 + (z - f)^2, \quad (4.94)$$

so that the wave front is described by

$$\ell_2 = 0, \quad (\ell_2)_\varphi = 0, \quad (\ell_2)_\psi = 0.$$

An explicit calculation yields

$$\begin{aligned} \ell^2 &= (t^2 \xi - t\Phi)^2 + (t^2 \eta - t\Psi)^2 + (1 + t + t^3 h - f)^2 \\ &= t^2 \Phi^2 + t^2 \Psi^2 - 2t^3 (\xi\Phi + \eta\Psi) + (1 + t)^2 - t^2 (\Phi^2 + \Psi^2) \\ &\quad - t^3 \Psi^2 + t^3 (h - \Phi^3 G) + O(t^4), \end{aligned}$$

so that at leading order $\ell_2 = t^3 \phi$, with ‘‘potential’’

$$\phi = h - \Phi^2 - \Psi^2 - 2(\Phi\xi + \Psi\eta) - \Phi^3 G(\Psi/\Phi) = 0.$$

Thus according to the condition $\ell_2 = 0$ we obtain

$$h = 2(\Phi\xi + \Psi\eta) + \Phi^2 + \Psi^2 + \Phi^3 G(\Psi/\Phi).$$

The extremal conditions $\phi_\Phi = \phi_\Psi = 0$ yield

$$\xi = -\Phi - 3\Phi^3 G + \Psi\Phi G', \quad \eta = -\Psi - \Phi^2 G',$$

respectively. Plugging this into the above we finally have

$$h = -\frac{1}{2}(\Phi^2 + \Psi^2) - 2\Phi^3 G(\Psi/\Phi), \quad (4.95)$$

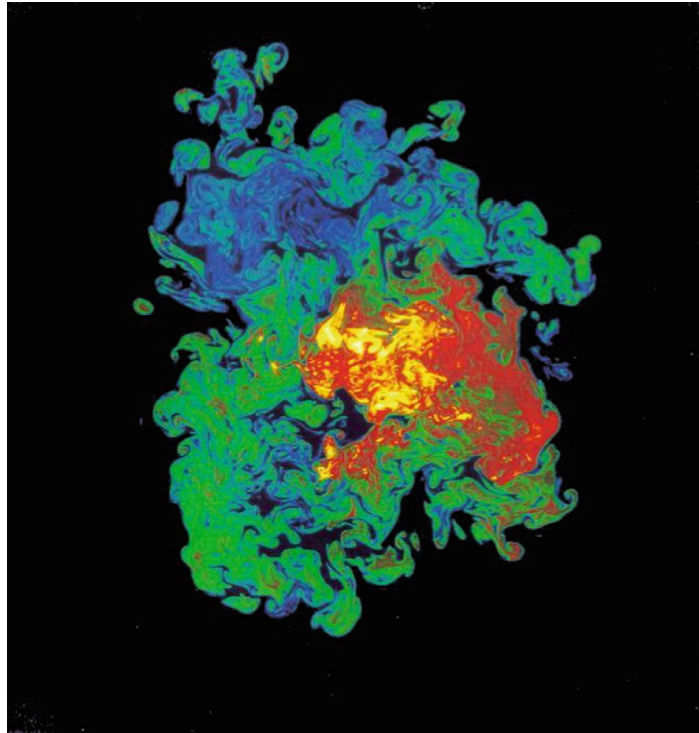
which corresponds to (4.87).

4.6 Spatial and Temporal Complexity

It is now time to tie together the different strands presented here. Without wanting to sound too grandiose, our ultimate aim is to describe a situation as shown in Fig. 4.25, which shows an example of turbulence. A characteristic of turbulence is a spatial superposition of disordered patterns over many scales.

To achieve something like that, we have to combine two different properties of the thin film equation: disorder, and unfolding into space. We consider the phase diagram, Fig. 4.26, to find appropriate values of n and m . We recall that the approximate

Fig. 4.25 A turbulent jet injected into another fluid at $\text{Re}=4.5 \times 10^3$ (Dimotakis, 2000), in a plane normal to the jet axis. The color map codes jet-fluid concentration



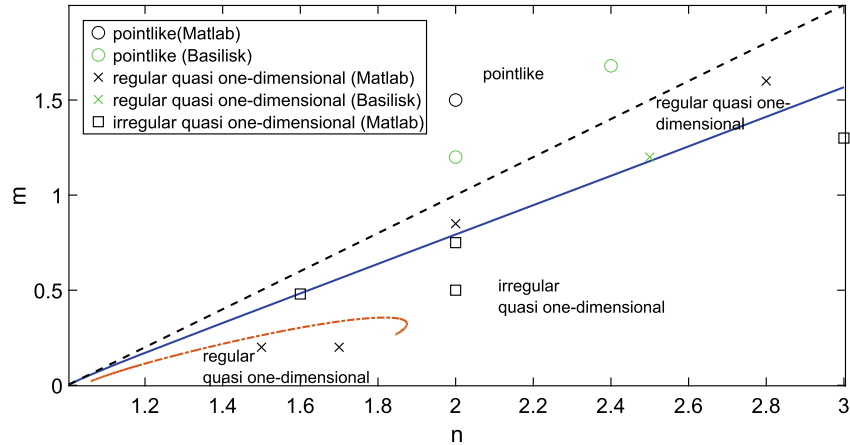


Fig. 4.26 Phase plane of the two-dimensional singularities of (4.10) (Dallaston et al., 2021a). The blue solid line is the border (4.58) between regular and complex behavior, the black dashed line is the border (4.62) between pointlike and quasi one-dimensional behavior. For smaller values of m , and $n > 1.87$ (below the orange dot-dashed line), there is a return to regular behavior. The symbols correspond to numerical simulations of (4.10) with initial condition (4.69)

condition $m > 0.8(n - 1)$ characterizes regular dynamics, as shown as the blue line, below which the self-similar dynamics become periodic, or even more complicated. The other important transition is marked by the dashed line $n = 1 + m$, below which the singularity is unfolded in the transverse direction. Thus below the blue line we have a combination of periodic or a-periodic instability, with new structures being created at smaller and smaller scales, and quasi-one-dimensional behavior, which unfolds this fractal structure into space.

An example of a simulation of (4.10) is shown in Fig. 4.27, where $n = 3$ and $m = 1.3$ (black square), so according to (4.58), we are in the irregular regime. On the left hand side, we show a perspective plot of $1/h$. While the peaks are smooth in the regular case, seen on the left of Fig. 4.18, they are now broken up into many smaller peaks, producing a spatially “spotty” behavior. In the y -direction, one observes the result of multiple instabilities, as seen on the right of Fig. 4.12 for the one-dimensional case. In addition, as x is detuned from 0.5, this irregular behavior is seen in different phases of its evolution, producing the hierarchy of peaks seen in Fig. 4.27. To emphasize the resulting complex spatial picture, on the right of Fig. 4.27 we also represent $1/h$ as a color contour plot in the plane.

As a further illustration, in Fig. 4.28 we show a snapshot of $1/h$ for a simulation of (4.10) with $n = 3$, $m = 1$ (black square in the phase diagram of Fig. 4.26), similar to that shown in Fig. 4.27. In that case, the one-dimensional dynamics is no longer merely periodic, but new structures keep being generated as one evolves toward smaller scales. Owing to the mechanism of unfolding, these new structures are translated into space, producing a spatially complex picture. As a result, one obtains a much more fractured picture than in the periodic case. This is clear especially on the right of Fig. 4.28, where a contour plot of $1/h$ reveals a spatially complex pattern.

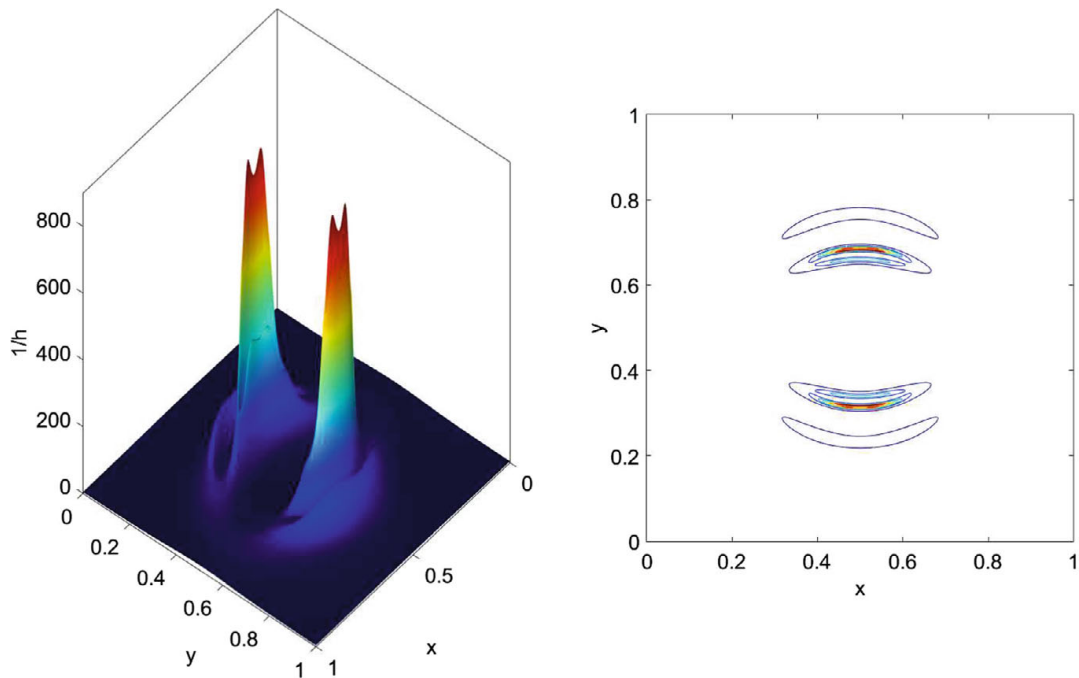


Fig. 4.27 Simulation of (4.10) with $n = 3$, $m = 1.3$ ($\alpha \approx 0.63$, $\beta \approx 0.72$), and initial condition (4.69), using $\epsilon_1 = 0.05$, $\epsilon_2 = 0.03$, $h_{\text{ref}} = 0.1$. A quasi one-dimensional, irregular singularity results, with periodic orbits. On the left a perspective plot of $1/h$ for $\tau = 8.7$. Along the one-dimensional front, one observes a sequence of instabilities. On the right, a contour plot of one of the peaks of $1/h$ (taken at the same time) shows the irregularity of the profile. The color, from blue to red, encodes $1/h$

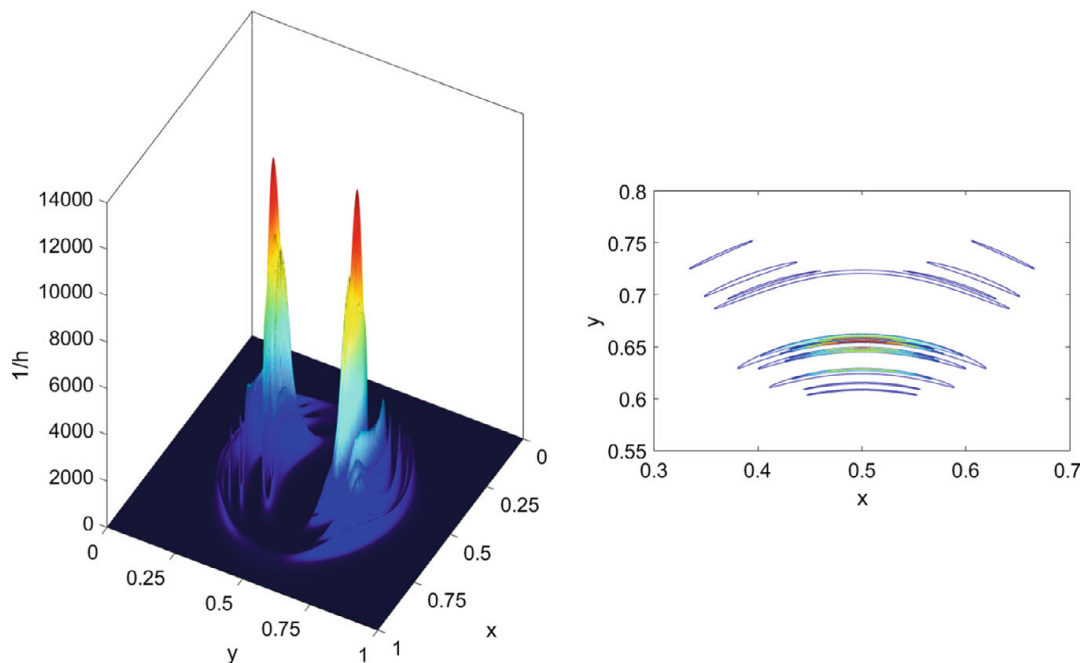


Fig. 4.28 Simulation of (4.10) with $n = 3$, $m = 1$, and initial condition (4.69), using $\epsilon_1 = 0.05$, $\epsilon_2 = 0.03$, and $h_{\text{ref}} = 0.1$, in the non-periodic regime. On the left, a perspective plot of $1/h$ at $\tau = 8.36$; on the right, a contour plot. The color code corresponds to Fig. 4.27

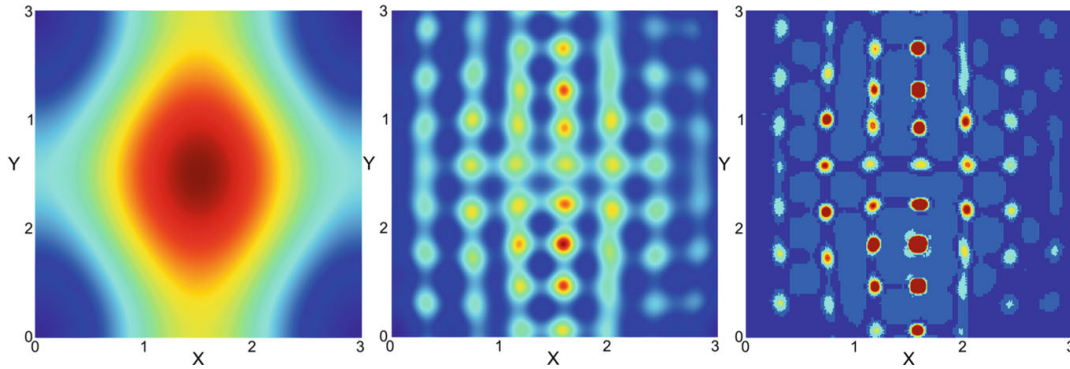


Fig. 4.29 Simulation of (4.10) with $n = 3, m = 1$ in a large domain $[0, 3] \times [0, 3]$, using Basilisk (Dallaston et al., 2021a). On the left, the initial condition $h_0(x, y) = 0.05 [1 - 0.05 \cos 2\pi(x/3 - 1/2)] [1 - 0.03 \cos 2\pi(y/3 - 1/2)]$, as a color plot of $1/h$. In the middle, a color plot of $1/h$ for $h_{\min} = 1.2 \cdot 10^{-2}$. Dark red corresponds to the smallest h , blue to the initial height. On the right, the grid generated by Basilisk, with blue corresponding to level 7 ($\Delta = 3/2^7 = 2.34 \times 10^{-2}$), and dark red to level 12 ($\Delta = 3/2^{12} = 7.32 \times 10^{-4}$)

A similar scenario, applied to singularity formation in the Euler equation, has been proposed some time ago by Pumir et al. (1992).

The non-periodic nature of the singularity also implies a sensitive dependence on initial conditions, as illustrated in Fig. 4.29. We show a larger spatial region, which encompasses more than 6 Rayleigh wavelengths $\lambda_R = 0.44$ (see (4.12)) of the most unstable mode of the initial film. As seen on the left of Fig. 4.29, the film is perturbed slightly on the scale of the entire domain, producing a non-uniform picture of decay; the initial condition is seen to have a fourfold symmetry. We use the Basilisk version of our code, owing to its capabilities of automatic refinement.

Since the evolution depends sensitively on the initial condition, slight changes in the initial condition translate into non-periodic behavior on the small scale. In the final image, the local singularity is seen in many different stages of its evolution, producing a very non-uniform picture (Fig. 4.29, middle, where $h_{\min} = 1.2 \cdot 10^{-2}$). Owing to small differences in how the refined grid is generated (see the image of the grid on the right), the fourfold symmetry of the initial condition is broken, and each local singularity looks different. We confirmed that a different choice of parameters for grid refinement leads to a qualitatively similar result, but with a different pattern of broken symmetry. We conjecture that the square pattern of rupture points is a result of the square grid used by Basilisk. We have also performed simulations in a large domain for the parameters of Fig. 4.18, for which the dynamics are regular. No symmetry breaking was observed, as expected.

Although our simulation of the large domain in Fig. 4.29 does not have sufficient resolution, each local rupture point will have the intricately folded structure seen at a higher resolution in Fig. 4.28. Thus non-periodic singular behavior leads to a very intricate superposition of structure in space, but also in scale: upon a change of magnification, new patterns are seen.

References

- Aarts, D. G., Lekkerkerker, H. N., Guo, H., Wegdam, G. H., & Bonn, D. (2005). Hydrodynamics of droplet coalescence. *Physical Review Letters*, *95*, 164503.
- Bertozzi, A. L., & Pugh, M. C. (1994). The lubrication approximation for thin viscous films: the moving contact line with a “porous media” cut off of van der Waals interactions. *Nonlinearity*, *7*, 1535–1564.
- Bertozzi, A. L., Brenner, M. P., Dupont, T. F., & Kadanoff, L. P. (1994). Singularities and similarities in interface flows. In L. Sirovich (Ed.), *Trends and perspectives in applied mathematics, volume 100 of applied mathematical sciences* (p. 155). Springer.
- Blossey, R. (2012). *Thin liquid films*. Springer.
- Burton, J. C., Rutledge, J. E., & Taborek, P. (2004). Fluid pinch-off dynamics at nanometer length scales. *Physical Review Letters*, *92*, 244505.
- Choptuik, M. W. (1993). Universality and scaling in gravitational collapse of a massless scalar field. *Physical Review Letters*, *70*, 9–12.
- Courrech du Pont, S., & Eggers, J. (2006). Sink flow deforms the interface between a viscous liquid and air into a tip singularity. *Physical Review Letters*, *96*, 034501.
- Courrech du Pont, S., & Eggers, J. (2020). Fluid interfaces with very sharp tips in viscous flow. *PNAS*, *117*, 32238.
- Craster, R. V., & Matar, O. K. (2009). Dynamics and stability of thin liquid films. *Reviews of Modern Physics*, *81*, 1131–1198.
- Dallaston, M. C., Fontelos, M. A., Herrada, M. A., Lopez-Herrera, J. M., & Eggers, J. (2021). Regular and complex singularities of the generalized thin film equation in two dimensions. *Journal of Fluid Mechanics*, *917*, A20.
- Dallaston, M. C., Tseluiko, D., Zheng, Z., Fontelos, M. A., & Kalliadasis, S. (2017). Self-similar finite-time singularity formation in degenerate parabolic equations arising in thin-film flows. *Nonlinearity*, *30*, 2647–2666.
- Dallaston, M. C., Zhao, C., Sprittles, J. E., & Eggers, J. (2021). Stability of similarity solutions of viscous thread pinch-off. *Physical Review Fluids*, *6*, 104004.
- Dimotakis, P. E. (2000). The mixing transition in turbulent flows. *Journal of Fluid Mechanics*, *409*, 69–98.
- Dong, J., Meissner, M., Faers, M. A., Eggers, J., Seddon, A. M., & Royall, C. P. (2018). Opposed flow focusing: evidence of a second order jetting transition. *Soft Matter*, *14*, 8344.
- Edgerton, H. E. (1977). *Stopping time: the photographs of Harold Edgerton*. Abrams.
- Eggers, J. (2012). Stability of a viscous pinching thread. *Physics of Fluids*, *24*, 072103.
- Eggers, J., & Fontelos, M. A. (2015). *Singularities: Formation, structure, and propagation*. Cambridge University Press.
- Eggers, J., & Suramlshvili, N. (2017). Singularity theory of plane curves and its applications. *European Journal of Mechanics B*, *65*, 107–131.
- Eggers, J., & Villermaux, E. (2008). Physics of liquid jets. *Reports on Progress in Physics*, *71*, 036601.
- Eggers, J., Fontelos, M. A., Leppinen, D., & Snoeijer, J. H. (2007). Theory of the collapsing axisymmetric cavity. *Physical Review Letters*, *98*, 094502.
- Eggers, J., Lister, J. R., & Stone, H. A. (1999). Coalescence of liquid drops. *Journal of Fluid Mechanics*, *401*, 293–310.
- Fontelos, M. A., & Wang, Q. (2021). Discrete selfsimilarity in the formation of satellites for viscous cavity break-up. *Physical Review Fluids*, *6*, 013201.
- Giga, Y., & Kohn, R. V. (1985). Asymptotically self-similar blow-up of semilinear heat-equations. *Communications on Pure and Applied Mathematics*, *38*, 297–319.
- Griffith, W. C., & Bleakney, W. (1954). Shock waves in gases. *American Journal of Physics*, *22*, 597.
- Hohlfeld, E., & Mahadevan, L. (2011). Unfolding the sulcus. *Physical Review Letters*, *106*, 105702.

- Kaneelil, P. R., Pahlavan, A., Xue, N., & Stone, H. A. (2022). Three-dimensional self-similarity of coalescing viscous drops in the thin-film regime. *Physical Review Letters*, *129*, 144501.
- Kitavtsev, G., Fontelos, M., & Eggers, J. (2018). Thermal rupture of a free liquid sheet. *Journal of Fluid Mechanics*, *840*, 555.
- Klopp, C., Trittel, T., & Stannarius, R. (2020). Self similarity of liquid droplet coalescence in a quasi-2d free-standing liquid-crystal film. *Soft Matter*, *16*, 4607–4614.
- Nye, J. (1999). *Natural focusing and fine structure of light: Caustics and wave dislocations*. Institute of Physics Publishing.
- Ockendon, J. R., Howison, S., Lacey, A., & Movvhan, A. (2003). *Applied partial differential equations*. Oxford University Press.
- Oron, A., Davis, S. H., & Bankoff, S. G. (1997). Long-scale evolution of thin liquid films. *Reviews of Modern Physics*, *69*, 931–980.
- Pantano, C., Gañán-Calvo, A. M., & Barrero, A. (1994). Zeroth order, electrohydrostatic solution for electrospraying in cone-jet mode. *Journal of Aerosol Science*, *25*, 1065.
- Pumir, A., Shraiman, B. I., & Siggia, E. D. (1992). Vortex morphology and Kelvin's theorem. *Physical Review A*, *45*, R5351–R5354.
- Reyssat, E., Lorenceau, E., Restagno, F., & Quéré, D. (2008). Viscous jet drawing air into a bath. *Physics of Fluids*, *20*, 091107.
- Taylor, G. I. (1934). The formation of emulsions in definable fields of flow. *Proceedings of the Royal Society of London A*, *146*, 501.
- Tjahjadi, M., Stone, H. A., & Ottino, J. M. (1992). Satellite and subsatellite formation in capillary breakup. *Journal of Fluid Mechanics*, *243*, 297.
- Witelski, T. P., & Bernoff, A. J. (2000). Dynamics of three-dimensional thin film rupture. *Physica D*, *147*, 155–176.
- Zhang, W. W., & Lister, J. R. (1999). Similarity solutions for van der Waals rupture of thin film on a solid substrate. *Physics of Fluids*, *11*, 2454–2462.